LAPPEENRANTA UNIVERSITY OF TECHNOLOGY

Faculty of Technology

Degree Programme in Energy Technology

Lauri Pyy

UTILIZATION OF PARTICLE IMAGE VELOCIMETRY IN PPOOLEX CONDENSATION EXPERIMENTS

Examiners: D.Sc(Tech) Heikki Purhonen

Professor D.Sc(Tech) Riitta Kyrki-Rajamäki

Instructor: D.Sc(Tech) Heikki Purhonen

TIIVISTELMÄ

Lappeenrannan teknillinen yliopisto

Teknillinen tiedekunta

Energiatekniikan koulutusohjelma

Lauri Pyy

PARTICLE IMAGE VELOCIMETRY –MITTAUSTEN TOTEUTTAMINEN PPOOLEX-LAUHTUMISKOKEISSA

Diplomityö

2012

94 sivua, 50 kuvaa, 14 taulukkoa ja yksi liite

Tarkastajat: Professori TkT Riitta Kyrki-Rajamäki

TkT Heikki Purhonen

Hakusanat: Particle Image Velocimetry –mittaustekniikka, PIV, termohydrauliikka, nestevirtaus, virtausnopeus, virtauskenttä, 3D PIV, laser, optinen mittausjärjestelmä

Particle Image Velocimetry, PIV, on optinen mittaustekniikka, jolla voidaan saada tutkittavasta virtauksesta nopeusinformaatiota. PIV-tekniikan avulla virtauksesta saadaan kaksi- tai kolmiulotteisia nopeusvektoreita tutkittavalta mitta-alueelta yhden pisteen sijasta. Mitattava virtaus voi olla joko kaasua tai nestettä. PIV-tekniikkaa sovelletaan nykyään laajalti virtausmittauksiin. PIV:llä on tarkoitus saada hankittua validointidataa laskennallisten virtausmallinnusohjelmien tarpeisiin Lappeenrannan teknillisen yliopiston, LUT, PPOOLEX-laitteiston ulospuhalluskokeiden mallinnusta varten. Tässä työssä esitellään PIV ja sen teoreettinen tausta. Työssä esitellään myös yksityiskohtaisesti kaikki PIV-mittauslaitteistoon luettavaksi kuuluvat osat ja kuvien analysoinnin matemaattinen tausta. Työhön kuului myös toimivan PIV-mittauslaitteiston kokoaminen ja testaus sekä sen sijoittamissuunnitelma PPOOLEX-laitteistoon.

Jo alustavissa kokeissa PIV:n havaittiin olevan hyvä lisä LUT:n Ydinturvallisuuden tutkimusyksikön mittauslaitteistoihin. Sijoittaminen ja asentaminen PPOOLEX-laitteistoon onnistui hyvin ja se todettiin toimivaksi, vaikkakin rajoituksia oli paljon. Kaikki PIV-mittalaitteiston osat toimivat ja ne todettiin tarkoituksenmukaisiksi. Työssä esitellyt tulokset ja huomiot ovat hyvä perusta PIV-mittauksille tulevaisuudessa.

ABSTRACT

Lappeenranta University of Technology

Faculty of Technology

Degree Programme in Energy Technology

Lauri Pyy

UTILIZATION OF PARTICLE IMAGE VELOCIMETRY IN PPOOLEX CONDENSATION EXPERIMENTS

Master's thesis

2012

94 pages, 50 figures, 14 tables and 1 appendix

Examiners: Professor D.Sc(Tech) Riitta Kyrki-Rajamäki

D.Sc(Tech) Heikki Purhonen

Keywords: Particle Image Velocimetry, PIV, thermal hydraulics, fluid flow, fluid velocity, velocity field, 3D PIV, laser, optical measuring system

Particle Image Velocimetry, PIV, is an optical measuring technique to obtain velocity information of a flow in interest. With PIV it is possible to achieve two or three dimensional velocity vector fields from a measurement area instead of a single point in a flow. Measured flow can be either in liquid or in gas form. PIV is nowadays widely applied to flow field studies. The need for PIV is to obtain validation data for Computational Fluid Dynamics calculation programs that has been used to model blow down experiments in PPOOLEX test facility in the Lappeenranta University of Technology. In this thesis PIV and its theoretical background are presented. All the subsystems that can be considered to be part of a PIV system are presented as well with detail. Emphasis is also put to the mathematics behind the image evaluation. The work also included selection and successful testing of a PIV system, as well as the planning of the installation to the PPOOLEX facility.

Already in the preliminary testing PIV was found to be good addition to the measuring equipment for Nuclear Safety Research Unit of LUT. The installation to PPOOLEX facility was successful even though there were many restrictions considering it. All parts of the PIV system worked and they were found out to be appropriate for the planned use. Results and observations presented in this thesis are a good background to further PIV use.

FOREWORD

First, I want to thank Mr. Heikki Purhonen for giving me opportunity to write this thesis. I also want to thank him from all the help and support considering this project. It was not always easy to make decisions when acquiring the system but I think sincerely that we succeed in it. Next, I want to thank Mrs. Riitta Kyrki-Rajamäki of all the helpful instructions considering the writing of this thesis. I also want to thank her for giving me pieces of advice before starting to write this thesis. It opened new opportunities for me that I never expected. I am forever grateful for that. I also want to thank Mr. John Boaler for his knowledge and guidance when planning and selecting appropriate PIV system and Mr. Rob Littlewood for all training and all instructions considering the use of it, you really helped me a lot. I am also grateful for all the employees of the Nuclear Safety Research Unit and Laboratory of Nuclear Engineering for all the help provided to me throughout this process.

My studies took maybe little longer than expected but it was truly the best time of my life. I want to thank my family for all the support they have given me during these years. I hope you can be proud of what I have become and what I have done. Without you I would never get this far in my life.

Last, I want to thank all my friends for giving me good times throughout my life. I think I am the luckiest guy in the World when it comes to having great friends and good people near me. And I sincerely hope most of you can celebrate this milestone in my life all around the World.

Contents

SYMBOLS

a	acceleration [m/s^2], interrogation area, diameter[m]
c	the speed of light in vacuum [299792458 m/s]
C	cross section [m^2]
d	diameter [m]
D	particle displacement vector
E	energy [J], irradiance [W/m^2]
f	focal length [m], frequency [Hz]
g	acceleration due to the gravity [9,81 m/s^2]
h	Planck's constant [~ 6,626·10^{-34} Js]
H	radiant exposure [J/m^2]
i	imaginary number [-]
I	Intensity [W/m^2]
K	extinction coefficient [-]
L	length of the medium [m]
m	integrer number [-]
M	magnification factor [-]
n	refractive index [-]
N	population of atoms [atoms/m^3]
$\tilde{n}$	complex refractive index [-]
P	power [W], [J/m^2]
q	normalized diameter [-]

R_C	mean background correlation function
R_F	noise term function
R_I	spatial autocorrelation function
R_{II}	spatial cross-correlation function
R_P	particle image self-correlation peak function
$\mathbf{s}$	separation vector
t	time [s]
T	time [s]
U	velocity [m/s]
V_0	transfer function [-]
W_0	weight function [-]
x	x-coordinate position [-]
$\mathbf{x}$	position vector in the image plane [-]
X	x-coordinate position in the object plane [-]
$\mathbf{X}$	position vector in the object plane
ΔX	horizontal interrogation volume dimension
y	y-coordinate position in the image plane [-]
Y	y-coordinate position in the object plane [-]
ΔY	vertical interrogation volume dimension
z	the distance between the image plane and the lens [m], z-coordinate position in the image plane [-]
Z	the distance between the lens and the object plane, z-coodinate position in the object plane [-]

Greek symbols

v	velocity of light in the medium [m/s], frequency [Hz]
$\mathbf{\Gamma}$	state of the tracer ensemble
ε	relative permittivity [-]
ρ	density [kg/m^3]
μ	dynamic viscosity [Pas], magnetic permeability [H/m]
λ	wavelength of the incident light [m]
δ	Dirac delta-function
τ	relaxation time [s], point spread function
φ	divergence of beam [rad]

subscripsts

0	Initial, optical
a	aperture
ave	average
f	fluid
g	gravitational
i	particle position
MPE	Maximum Permissible Exposure
N	number of tracer particles
p	particle
peak	peak power
s	relaxation

S	scattering
τ	particle diameter
XY	maximum value in *XY* direction
Z	maximum value in *Z* direction

abbreviations

Ar^+	Argon-ion
BFS	Bubble fluid solution
BWR	Boiling Water Reactor
CCD	Charge-coupled design
CFD	Computational fluid dynamics
CCTS	Centrifugal compressor test station
Cu	Copper-vapor
Cr^{3+}	Chromium-ion
CMOS	Complementary Metal Oxide Semiconductor
DEHS	Di-ethyl-hexyl-sebacate
EU	European Union
FOV	Field of view
He-Ne	Helium-neon
IEC	International Electrotechnical Commission
LIF	Laser-induced fluorescence
LUT	Lappeenranta University of Technology
MPE	Maximum Permissible Exposure

Nd	Neodym
NPP	Nuclear Power Plant
NUCPRI	Nuclear Power Research Infrastructure
PIV	Particle Image Velocimetry
SAFIR	Safety of Nuclear Power Plants
SNR	Signal-to-noise ratio
YAG	Yttrium-aluminum-garnet
YLF	Yttrium-lithium-fluoride

1 INTRODUCTION

Particle Image Velocimetry, PIV, is a way to visualize and measure flow velocity properties in three dimensions. PIV is nowadays widely applied for flow field studies. The validation of modern Computational Fluid Dynamics, CFD, calculation programs require good quality measurement data of flow properties. With PIV it is possible to obtain the needed measurement data with sufficient temporal and spatial information. This thesis is part of the Finnish Academy funded project NUCPRI, Nuclear Power Research Infrastructure and SAFIR, the Finnish National Research Programme on Safety of Nuclear Power Plants and it is done for the Nuclear Safety Research Unit of Lappeenranta University of Technology. The work included selection and successful testing of functional PIV system for the Nuclear Safety Research Unit.

In this thesis PIV with its basic working principles and the basic sub systems that can be thought of being a PIV system are introduced first. It is followed with thorough description of tracer particles and their properties and the most typical ways to generate seeding for the flow being measured. Lasers and physics behind creating laser light are presented next. Also the most popular laser types are described. Lasers as light sources with description of optics that are used to create light sheet for illuminating the measured flow follows. Nowadays imaging is done digitally and typical digital image recording media as well as the statistical and mathematical evaluation of digital images are described in the thesis. For the more practical aspect of the thesis the applications utilizing PIV are described briefly and the acquired PIV system in detail. Emphasis is put in describing positioning of PIV system to PPOOLEX facility which is the main application for acquired PIV system. Laser safety is important part when operating high powered lasers as in PIV systems so protective measures and possible hazardous situations are presented. Finally, the actual experimental PIV system setup for PPOOLEX is presented as well as obtained results from preliminary PIV experiment in PPOOLEX. Last, conclusions with suggestions for future improvements are presented.

2 INTRODUCTION TO PIV SYSTEMS

Particle Image Velocimetry, PIV is, in principle, a technique to obtain velocity information out of a flow by utilizing light and optics. In practice, PIV system is built out of sub systems. For operational system a laser, light sheet optics and mirror to create an illuminating light sheet, illuminating particles, imaging optics and a flow is needed to make a PIV system. A typical experimental arrangement for PIV measurement is shown in figure 1. (Raffel et al. 2007, 3-4)

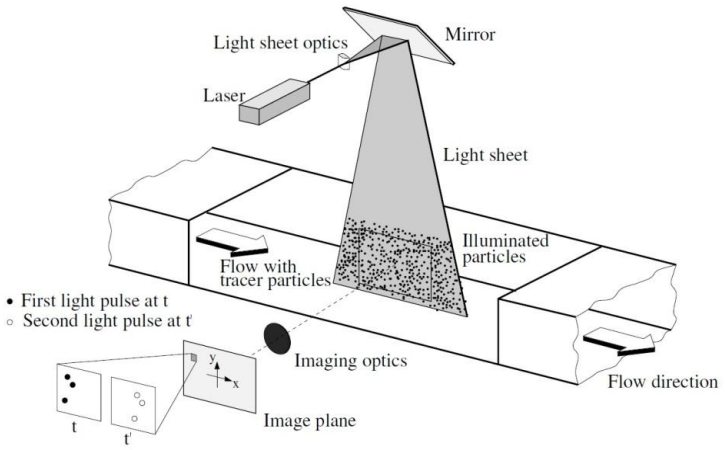

Figure 1. A typical experimental arrangement for PIV measurement (Raffel et al. 2007, 4)

Firstly, a laser beam is generated and through light sheet optics and a mirror the illuminating light sheet is created. The measured flow is seeded with tracing particles, for example glass spheres that reflect light, which the light sheet illuminates. Imaging optics, usually on a high-resolution digital camera or normal film camera, is then used to capture a picture out of the illuminated tracing particles. To obtain information about the flow field, two separate laser beams and pictures need to be taken and be compared. The comparing of the pictures is done with computer software that is able to analyze the information held by the pictures, e.g. the velocity field of the flow. It is assumed that the tracer particles move with local flow velocity between the two illuminations. In figure 2 is shown the basic principles of a PIV measurement. (Raffel et al. 2007, 3-4; Westerwheel J. 1993, 32)

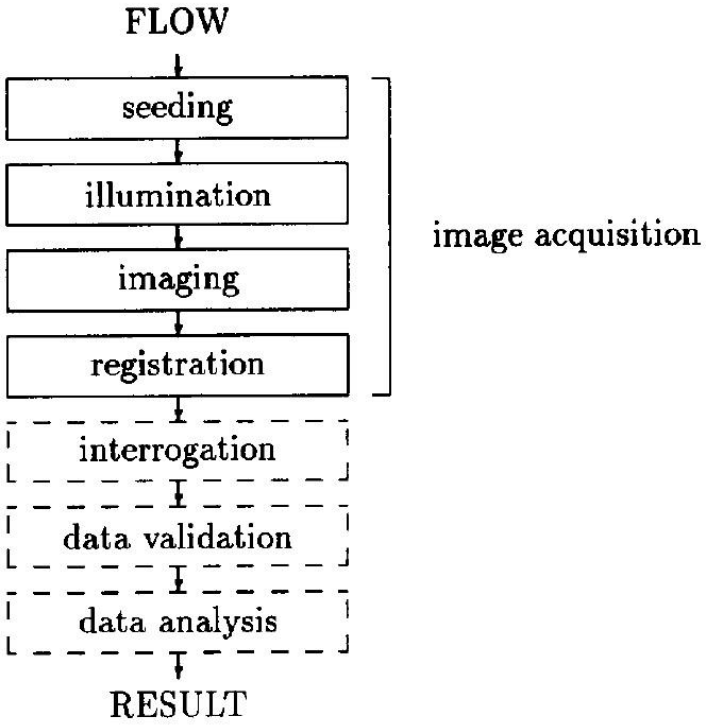

Figure 2. The basic principle of a PIV measurement (Westerwheel J. 1993, 32)

For evaluation purposes, the digital PIV recording is divided in smaller subareas. Those subareas are called “interrogation areas”. By means of statistical methods, the local displacement vector for the images of tracer particles of the first and second illumination is determined. It is also assumed that between two illuminations all particles have moved homogenously within the interrogation area being analyzed. By analyzing how tracer particles have moved taking the time delay between pictures in consideration, a velocity vector can be determined within the interrogation area. And by combining all individual vectors from all individual interrogation areas, the velocity field can be obtained. By using modern digital camera equipment, like CCD camera with up to 1000x1000 sensor elements, over 100 PIV recordings per minute rate can be achieved. For higher speed recording CMOS cameras are used. The rate is then in the kilohertz-range. (Raffel et al. 2007, 4)

With normal table top computers several thousand individual velocity vectors can be processed in a second. PIV can be also used for online monitoring. For online

monitoring changes in interrogation area size and processing algorithms need to be done. (Raffel et al. 2007, 4-5)

The biggest improvement in PIV in last decades has been the transformation to digital techniques in recording and evaluation of data. Due to these improvements, PIV has achieved a state that it is regularly applied in aerodynamic research and other investigations of fluid or air flow. (Raffel et al. 2007, 4-5)

3 TRACER PARTICLES AND THEIR PROPERTIES

The tracer particles that are used for seeding of the flow have two main characteristics that they should fulfill. Firstly, the particles should, of course, scatter light from the created light sheet. Secondly, the tracer particles should track the motion of the flow as closely as possible. For light scattering purposes it is feasible to use as big particles as possible. And for the flow's motion tracking purposes it would be feasible to use as small particles as possible depending on the density of the tracer particle. When using small particles the light scattering features are not good and when using big particles they might not track the flow motion correctly. Needless to say that when choosing the tracer particles some sort of compromise has to be found between those two qualities mentioned.

3.1 Flow properties of tracer particles

Gravitationally induced velocity, U_g, when the densities of fluid and tracer particle do not match can be derived from Stoke's drag law. If particles are assumed to be spherical in a viscous flow and the Reynold's number is very low, the gravitationally induced velocity, U_g, can be resolved from equation (1):

$$U_g = d_p^2 \frac{(\rho_p - \rho_f)}{18\mu_f} g, \quad (1)$$

where d_p is the diameter of the particle, ρ_p is the density of the particle, ρ_f is the density of the fluid, μ_f is the dynamic viscosity of the fluid and g is the acceleration due to the gravity. (Raffel et al. 2007, 15)

The velocity lag of a particle in a continuously accelerating fluid is analogous to equation (1) and can be resolved from equation (2):

$$U_s = U_p - U_f = d_p^2 \frac{(\rho_p - \rho_f)}{18\mu_f} a_f, \tag{2}$$

where Up is the particle velocity, U_f is the fluid velocity and a_f is the acceleration of the fluid. It can be seen from the equation (2) that due to the difference in density between the particle and the fluid, the diameter of the particles should be very small in order to ensure good tracking of the fluid motion. Or the density of the particle should be close to the fluid's density. (Raffel et al. 2007, 15)

If the density of the particle is much greater than the fluid density the step response of U_p typically follows exponential law. Time-dependent particle velocity can be resolved from equation (3):

$$U_p(t) = U\left[1 - e^{\left(-\frac{t}{\tau_s}\right)}\right], \tag{3}$$

where t is time and τ_s is relaxation time which can be resolved from equation (4):

$$\tau_s = d_p^2 \frac{\rho_p}{18\mu_f} \ . \tag{4}$$

If the Stoke's drag does not apply or the fluid acceleration is not constant the equations of the particle emotion becomes more difficult to solve. The relaxation time, τ_s, remains nevertheless as a convenient measure for the tendency of particles to attain velocity equilibrium with the fluid. (Raffel et al. 2007, 16)

3.2 Light scattering properties of tracer particles

Tracer particle's light scattering properties are an important factor since the obtained particle image density and contrast of the PIV recording depends on it. There are two ways to increase the scattering light power. Either the output power of the laser, or other light source, is increased, or by correctly choosing the tracer particles. For small particles, the scattering light power is a function of the ratio of the refractive index of the particles comparing to surrounding medium and the size, shape and orientation of the particles. (Raffel et al. 2007, 18)

The refractive index of a medium is very important factor in many situations when optics is in question. The refractive index for a medium can be solved with equation (5):

$$n = \frac{c}{v} \ , \tag{5}$$

where n is the refractive index of a medium, c is the velocity of light in vacuum and v is light's velocity in the medium. An alternative way to solve medium's refractive index is presented in equation (6):

$$n = \sqrt{\varepsilon\mu} \ , \tag{6}$$

where ε is medium's relative permittivity and μ is the magnetic permeability. In the medium that absorbs or scatters radiation when it's passing through it, the refractive index is a complex function of the frequency of lightwave, presented in the equation (7):

$$\tilde{n} = n - iK \ , \tag{7}$$

where $\tilde{n}$ is the complex refractive index, i is the imaginary number and K is an extinction coefficient. (Kasap S.&Capper P. 2006, 47)

Also the polarization and observation angles have an effect to the scattering light power. For spherical particles with diameters, d_p, larger than the wavelength of the

incident light λ, Mie's scattering theory can be applied. The Mie's scattering is characterized by the normalized diameter which is defined in the equation (8):

$$q = \frac{\pi d_p}{\lambda} , \tag{8}$$

where q is the normalized diameter and λ is the wavelength of the incident light. (Raffel et al. 2007, 18)

The intensity scales for two oil particles with different diameters according to Mie's theory are shown in figures 3 and 4. (Raffel et al. 2007, 18)

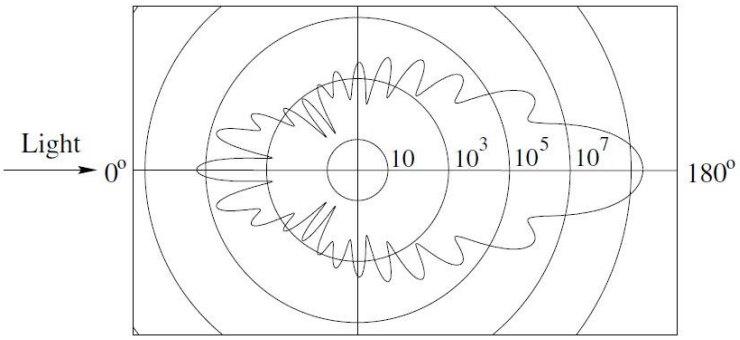

Figure 3. The light scattering intensity scale of a 1 μm oil particle in air (Raffel et al. 2007, 18)

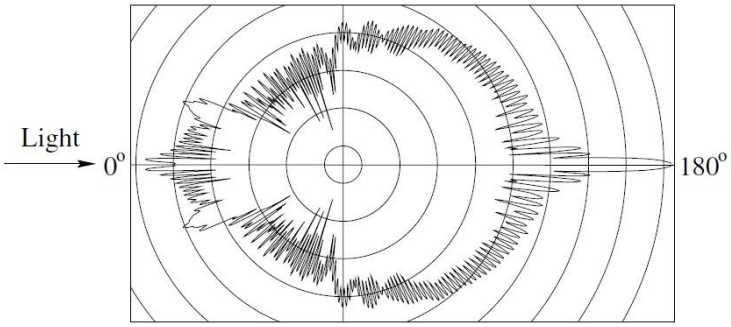

Figure 4. The light scattering intensity scale of a 10 μm oil particle in air (Raffel et al. 2007, 19)

The intensity scale in the figures 3 and 4 is logarithmic and the difference between neighboring circles differ by the factor of 100. The wavelength of the incident light is 532 nm. As mentioned before, the polarization and observation angles have an effect to the scattering light power of the tracer particle and it is clearly shown in figures 3 and 4. As well as what is the effect of the size of the tracer particle. It would be

beneficial to record the scattered light from forward direction, e.g. at 180°, but the limited depth of field forces usually to use the direction at 90°. When using two cameras for recording the direction at 90° is also beneficial as the cameras can be installed perpendicular to each other while having almost the same scattering intensity. (Raffel et al. 2007, 19-20)

When the fluid is water the particle size must be enlarged due to the fact that the refractive index of water is considerably larger than that of air. But as the density of water is also larger than that of air, it is acceptable. The densities of the tracer particles used for water flows are closer to water density and thus more naturally buoyant meaning that the flow properties are better even with larger particle size. The scattering intensity scales according to Mie's theory of different diameter glass particles in water are shown in figures 5 to 7. (Raffel et al. 2007, 20)

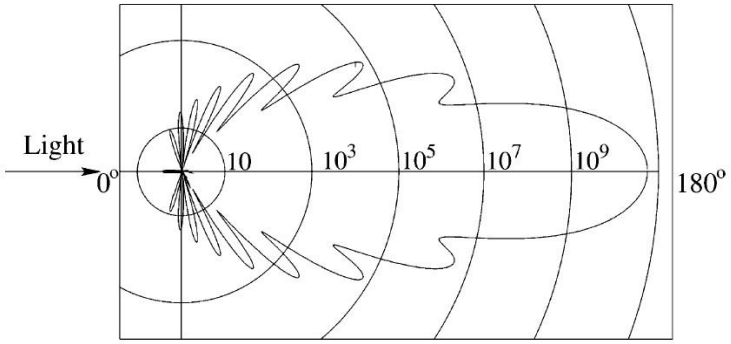

Figure 5. The light scattering intensity scale of a 1 μm glass particle in water (Raffel et al. 2007, 20)

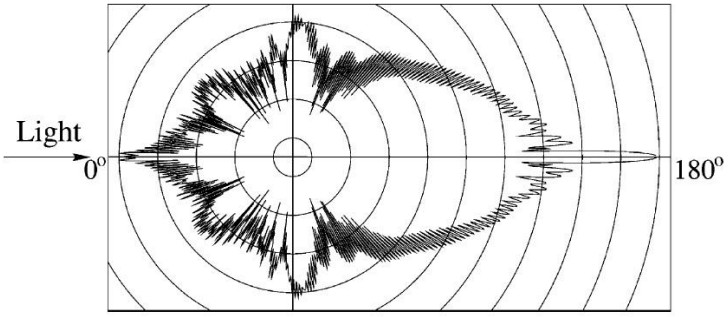

Figure 6. The light scattering intensity scale of a 10 μm glass particle in water (Raffel et al. 2007, 20)

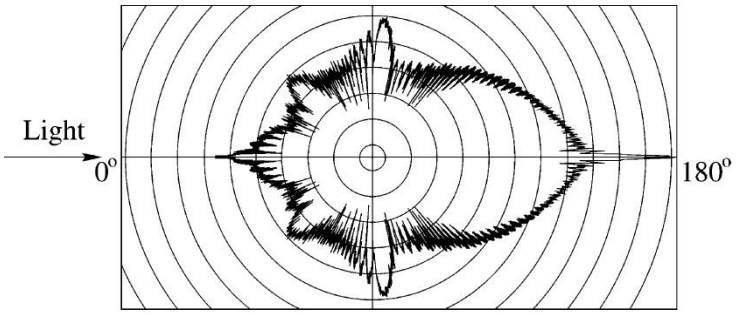

Figure 7. The light scattering intensity scale of a 30 μm glass particle in water (Raffel et al. 2007, 20)

The scales are the same in each figure and the wavelength of the incident light is 532 nm. All the Mie's scattering diagrams presented before show that the light is reflected in all directions. Because the light is scattered in every direction, the particles in the light sheet scatter the light of other particles as well, e.g. multiscattering occurs. In heavily seeded flows, multiscattering increases the scattering intensity of a single particle. In other words, the enlargement of particle size is not the only way for increasing scattering intensity. Also the particle density, e.g. the amount of particles in one interrogation area, can be enlarged. The limitation for the particle density is restricted by the amount of background noise of the obtained image. (Raffel et al. 2007, 20-21)

The light scattering capability of a single tracer particle can be solved from equation (9):

$$C_S = \frac{P_S}{I_0}, \tag{9}$$

where C_S is the light scattering cross section, P_S is the total scattered power and I_0 is the intensity of the incident particle. Scattering cross section is heavily relied on the ratio between the diameter of tracer particle and laser wavelength as can be seen in figure 8. (Melling A. 1997, 1406-1407)

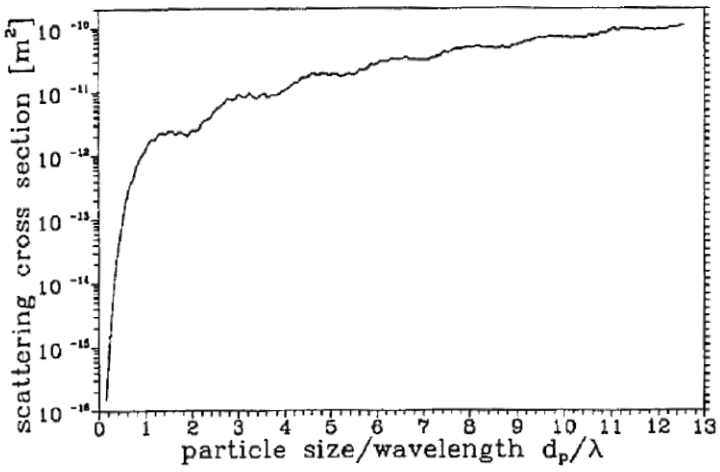

Figure 8. The development of scattering cross section comparing to the ratio of particle size and laser wavelength (Melling A. 1997, 1407)

In figure 8 the value of the scattering cross section is between $10^{-16} – 10^{-10}$ m^2 and the refractive index n = 1.6. To obtain good scattering properties it is clearly seen that the tracer particles have to be in diameter at least the same as the laser's wavelength. (Melling A. 1997, 1406-1407)

3.3 Seeding of the flow and seeding material

Seeding particles are normally added to the measured flow due to the fact that reflecting particles are not usually naturally present in the measured flow. By seeding the flow with tracer particles the image contrast and the sizes of particles can be controlled as well. When measuring a liquid flow a proper seeding is easily achievable by adding solid particles into the flow and mixing it so that it forms a homogenous distribution of tracer particles. The seeding for a liquid flow can also be done by adding liquid or gaseous particles into the flow. In table 1 typical seeding particles for liquid flow measurements are presented with their type and mean diameter. (Raffel et al. 2007, 21)

Table 1. Seeding materials for liquid flows (Raffel et al. 2007, 21)

Type of the particle	Material	Mean diameter, d_p [μm]
Solid	Polystyrene	10-100
	Aluminium flakes	2-7
	Hollow glass sphere	10-100
	Granules for synthetic coatings	10-500
Liquid	Different oils	50-500
Gaseous	Oxygen bubbles	50-1000

As seen from the table 1 all particles presented fulfill the Mie's scattering criteria if the laser used for producing light would emit light in the visible light area ($d_p > \lambda$). When seeding a gas flow the density difference between the tracer particles and the gas flow is imminent and thus the velocity lag between the particle and the flow is significant. The main reasons why a gas flow is hard to seed are:

- liquid particles, or droplets, tend to evaporate easily
- solid particles tend to agglomerate and they are hard to disperse
- injecting particles into the flow without significantly disturbing it is hard to achieve if a homogenous distribution is wanted to be achieved
- turbulence of the gas flow is usually not sufficient to mix the particles into the flow.

Typical seeding material for gas flows are presented in table 2. (Raffel et al. 2007, 22-23)

Table 2. Seeding materials for gas flows (Raffel et al. 2007, 23)

Type of the particle	Material	Mean diameter, d_p [μm]
Solid	Polystyrene	0.5-10
	Alumina Al_2O_3	0.2-5
	Titania TiO_2	0.1-5
	Granules for synthetic coatings	10-50
	Glass micro-spheres	0.2-3
	Glass micro-balloons	30-100
	Dioctylphathalate	1-10
	Smoke	<1
Liquid	Different oils	0.5-10
	Di-ethyl-hexyl-sebacate (DEHS)	0.5-1.5
	Helium-filled soap bubbles	1000-3000

The diameters of the seeding particles for the gas flow are drastically smaller than when seeding a liquid flow. As the particles are denser than the flow, the diameters have to be reduced to achieve appropriate flow properties. The lower ends of diameters in some particles do not fulfill the Mie's scattering criteria anymore. (Raffel et al. 2007, 22-23)

In gas flow where particles are relatively small in diameter and when there is the need for decreasing observation area for increasing optical resolution in the investigation, the diameters of tracer particles have to be decreased substantially. The regime where the diameter of the tracer particle is much smaller than the wavelength of the reflected light, $d_p << \lambda$, is called Rayleigh's regime. When the particle size is closing the Rayleigh's regime the recording of the particle images becomes extremely hard. When facing such conditions it is feasible to use epi-fluorescence imaging which is achieved with the help of fluorescent particles and by using an optical wavelength-specific long-pass filter to remove the background light. The only

light recorded is the light fluoresced by the particles. Although fluorescent particles offer good option for improving smaller observation area measurements, e.g. PIV measurements in micro scale, there are still problems with gas flows. Commercially available fluorescent particles are usually in aqueous suspension meaning that the same problems that are present with other aqueous solution are present with those as well. Commercially available fluorescent dry particles are available in larger sizes, d_p > 7 μm. Drying the aqueous suspension is possible but the electrical surface charge of the dried particles allows them to stick in flow boundaries and to each other. (Raffel et al. 2007, 22-23)

3.4 The generation of seeding particles

As mentioned before, seeding for liquid flows are easier to achieve. Usually the generation of scattering particles for liquid flow is done by mixing particles in powder form or as a suspension into the flow whereas gas flows need some sort of generator for the production of scattering tracer particles. Gas flows are commonly seeded either with liquid droplets or with solid particles. The reasons why gas flow is harder to seed are presented in previous chapter. The generators used for generation, whether it's gas or liquid flow, should produce monodisperse particles at a high enough rate. The production rate should be high enough to achieve at least 15 particles per interrogation area. (Melling A. 1997, 1412)

There are numerous techniques for generating tracer particles for gas flows. The most commonly used techniques are dry powder dispersing by fluidized beds or by air jets, liquid evaporation and precipitation afterwards in condensation generators or generating liquid droplets directly in atomizers. Atomizers can also be used to disperse solid particles suspended in evaporating liquids or to generate droplets out of a high vapor pressure liquid that is mixed in low vapor pressure liquid that evaporate prior to the entry of a test section. For wind tunnels the seeding can be achieved with using condensation or smoke generators or by injecting monodisperse polystyrene or latex particles in water-ethanol mix. (Raffel et al. 2007, 23)

3.4.1 The generation of droplets by condensation

The simplest way to generate seeding is by condensation. Usually oil is heated into vapor and let to condensate to fine droplets in the gas flow. The downside of its simplicity is that the generation rate of seeding is hard to regulate making it unsteady and the distribution of droplet size varies. Also the attained concentration is low. (Melling A. 1997, 1412)

3.4.2 The generation of droplets by atomization

The most used technique for generating droplets is a Laskin atomizer. The principle for a Laskin atomizer is simple. First liquid is drawn from a supply reservoir by a low static pressure of an entraining gas jet forming a thin film which is then ruptured by the high velocity gas flow into individual droplets. With Laskin atomizer the particle concentrations as high as 10^9-10^{10} m^{-3} can be achieved. A typical Laskin atomizer is presented in figure 9. (Melling A. 1997, 1412)

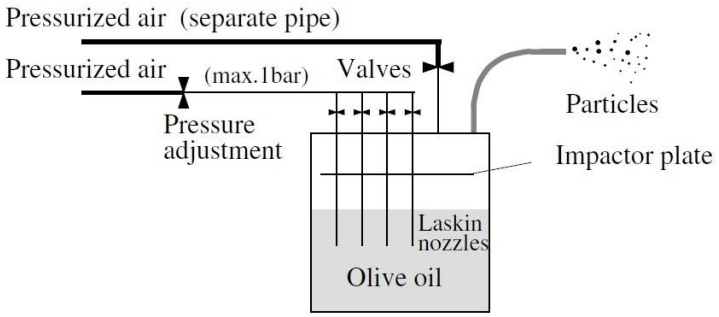

Figure 9. A Laskin atomizer (Raffel et al. 2007, 24)

The main parts of a Laskin atomizer are two separate pressurized air inlets with regulation valves, Laskin nozzles that are in the end of the air inlet that is in touch with the liquid that the droplets are generated from, a cylindrical container which is closed, one outlet for produced droplets and an impactor plate. (Raffel et al. 2007, 24)

The air inlet that has the Laskin nozzles in the end are closed. The other air inlet is in the top part of the container on top of the impactor. The droplets are produced by injecting pressurized air through the Laskin nozzles. A sketch of a typical Laskin nozzle with its measures is presented in the figure 10. (Raffel et al. 2007, 24)

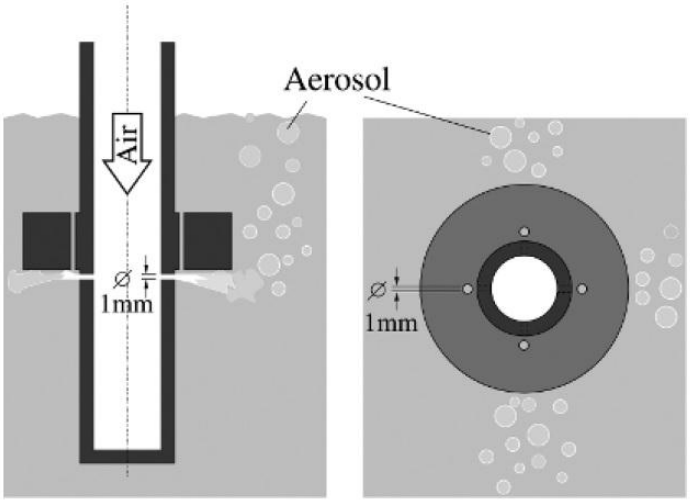

Figure 10. A typical Laskin nozzle (Raffel et al. 2007, 24)

The concentration of generated droplets can be adjusted with the valves of each air inlet that is leading to Laskin nozzles or by decreasing or increasing the air flow from the other air inlet that is attached to the top of the container. The Laskin nozzles create air bubbles to the liquid. The pressure difference between the compressed air of the air inlet and the outlet is between 0.5-1.5 bar which is measured by pressure gauges inside the container and the air inlet. Due to the shear stress induced by the small sonic jets, small droplets are generated and carried inside the bubbles towards the oil surface. The impactor plate is constructed so that a small gap is left between the end of the impactor plate and the wall of the container. The impactor plate separates too large particles from the created aerosol flow. Then generated droplets exit from the outlet to the measured flow. The size of the produced droplets depends mainly on the liquid used for the generation. The pressure of the air injected through Laskin nozzles has only slight dependency to the droplet size. Usually different vegetable oils, like olive oil, are used. By using vegetable oils, no or very little health risks are involved. Generally any kind of toxic liquid or a liquid that is not dissolvent to water is not recommended. When using vegetable oils for the generation of

droplets, the distribution is polydisperse which can be considered a down side. The mean diameter around 1 μm can be achieved by using vegetable oils. (Raffel et al. 2007, 24)

3.4.3 The generation of solid particles from powders

Sometimes the conditions of the gas flow might not be feasible for the droplet-based seeding, e.g. the temperature of the flow can be too high or the flow environment can be reactive among other reasons. Substances used for the generation of solid particles from powders are usually metal oxide powders which are well suited for harsh flow environments because of their inertness, high melting point and rather low cost. (Raffel et al. 2007, 25)

The aerosol of seeding particles is most commonly generated in fluidized beds. A typical fluidized bed is presented in the figure 11. (Raffel et al. 2007, 27)

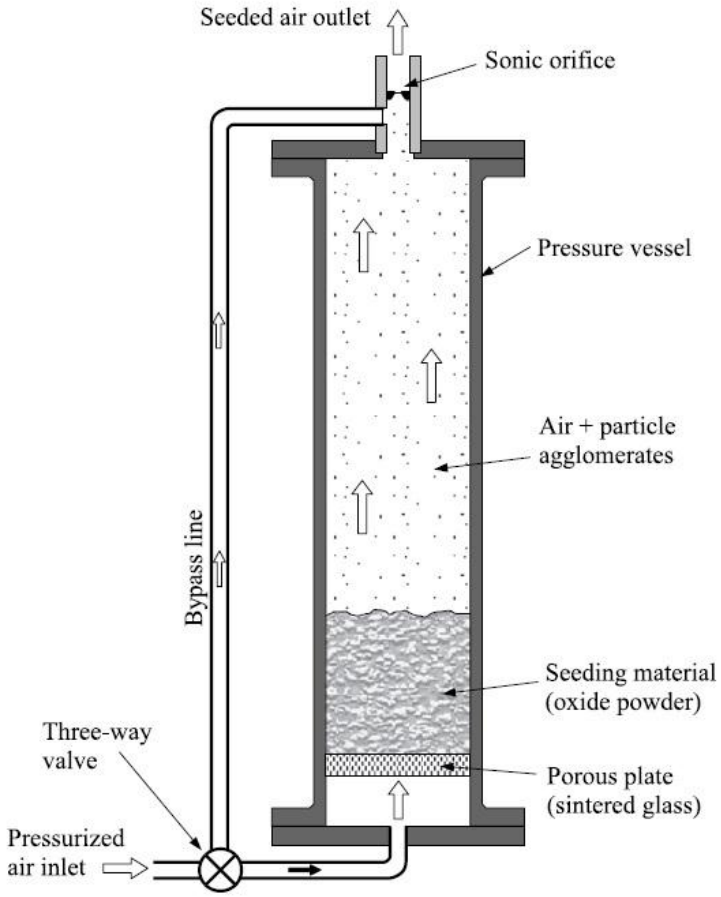

Figure 11. A fluidized bed for seeding of a gas flow from powder (Raffel et al. 2007, 27)

The principle of a fluidized bed is simple. First pressurized air is led to the bottom of the bed consisting of seeding material. Pressurized air and seeding material form aerosol that is used for seeding of the gas flow. The aerosol is drawn into the measured gas flow from the top. Extra air is led to the air outlet to break up the larger agglomerates of the generated aerosol. (Raffel et al. 2007, 25-26)

The factors that affect the generated particle size are:

- the humidity of the gas used to fluidize the bed
- the moisture content of the powder
- the mass rate of the flow through the bed.

Smooth, dry and hard particles disperse more easily than rough, soft and moist particles. In that sense it is more feasible to use as dry powder as possible but it has

to be taken into consideration that electrostatic forces might agglomerate particles and restrict the dispersion. Also the flow through the bed should be low enough so that no slugs or bubbles are formed making the bed density non-uniform. The non-uniform bed density leads to an erratic rate of generation. (Melling A 1997, 1413-1414)

For successful operation of a fluidized bed:

- the seeding powder should be kept dry or it should be heated before to remove excess moist out of it
- dry air or nitrogen should be used to operate the seeder
- short supply lines between the seeder and the facility should be used to prevent the formation of agglomerates
- additional carrier air should be used to reduce the relative seeding concentration. (Raffel et al. 2007, 26-27)

For further improving steady distribution of concentration and the steady particle size, two-phase beds can be used. In two-phase beds the bed consists of the seeding material and bigger beads of nickel, bronze or glass in diameter of 100-200 μm. When injecting air to the bottom of the bed, seeding material starts moving upwards between the beads. As beads are heavier than the seeding particles, the beads form the fluidized bed and the seeding particles can move freely between the beads. When seeding particles move between the beads the agglomerates are broken down thus achieving the steadier particle size and the distribution of concentration. The seeding particles are elutriated from the bed by rising gas bubbles which burst at the surface of the bed, releasing the particles. A sketch of a two-phase bed is presented in the figure 12. (Melling A 1997, 1413-1414)

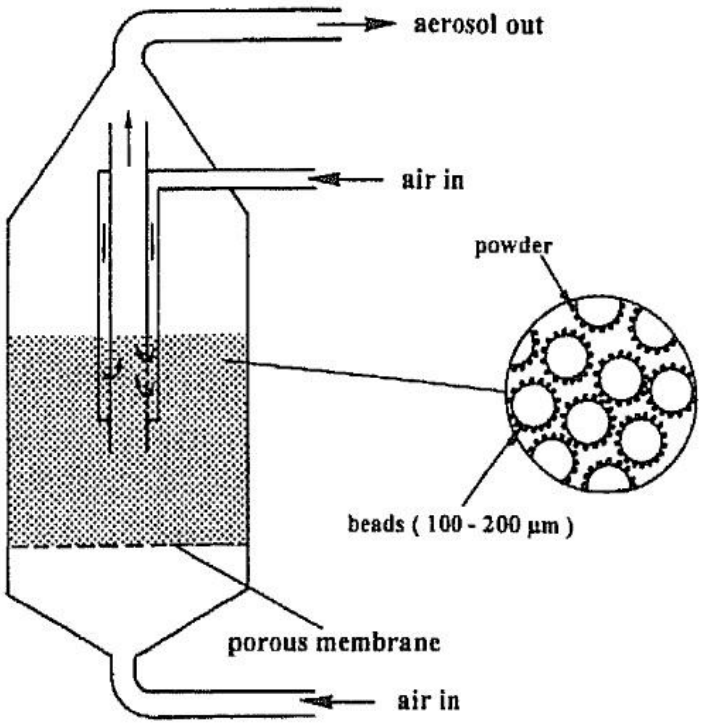

Figure 12. A two-phase fluidized bed (Melling A 1997, 1414)

3.4.4 The generation of solid particles by atomization

The biggest advantage of generating solid particles by atomization is that a steady concentration can be achieved. Usually solid particles are in a suspension with volatile solvent or other suspending liquid. Normally the sizes of particles are polydisperse because the size depends on the initial droplet diameter and the concentration of the solution. Well below 1 µm in size of particles can be achieved and the generation can be done with same technique as the generation of droplets by atomization presented in the chapter 3.4.2. (Melling A 1997, 1413)

3.4.5 The generation of helium-filled soap bubbles

One limitation for the field of view, FOV, is the scattering efficiency of the tracer particles. With oil droplets in diameter of 1 µm the obtained FOV is around

1000·750 mm^2 with commonly used laser. For enlarging the FOV it would be feasible to use larger particles. But enlarging particle size also makes them not neutrally buoyant because of the increased mass which is required for seeding a gas flow. One way to tackle this issue is to use soap bubbles filled with helium gas. Helium gas compensates the weight of the soap and naturally buoyant particles in diameters of 1-3 mm can be generated. A schematic drawing of a generator for helium-filled soap bubbles is presented in the figure 13. (Raffel et al. 2007, 27-28)

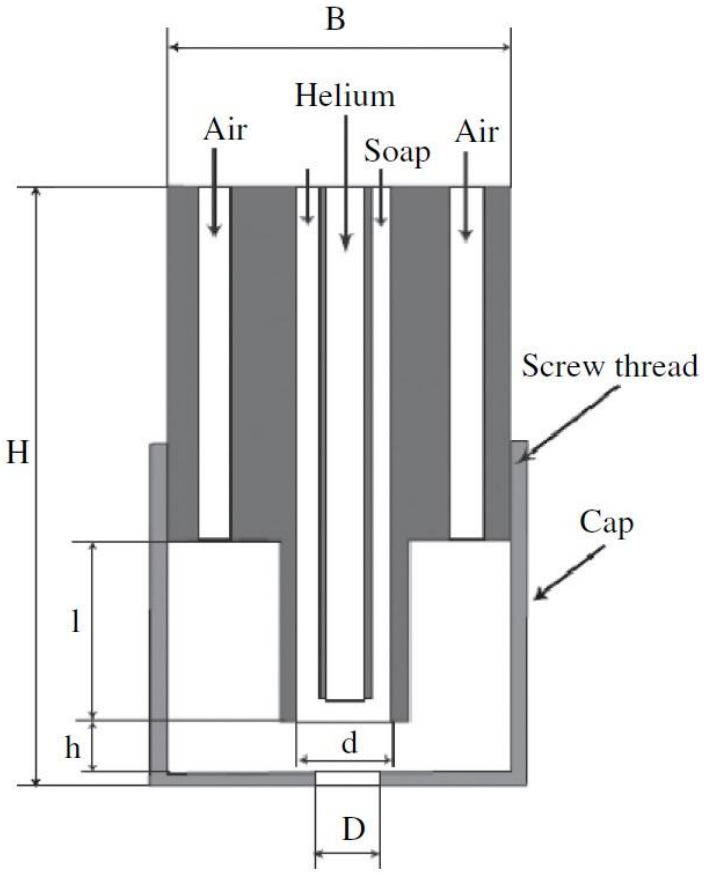

Figure 13. A nozzle for generating He-filled soap bubbles (Raffel et al. 2007, 26)

In the nozzle helium flows from the central pipe which is inside a bigger pipe that contains the bubble fluid solution, BFS. The BFS is usually a mix of water, glycerin and soap. The helium-filled soap bubbles are generated in the end of the BFS pipe and their separation from the tubes is driven by the additional air pipes. The factors that impact the generation of neutrally buoyant bubbles are the pressure of helium, air-pressure, BFS flow rate and the distance between nozzle gap and tubes (marked as *h* in the figure 13). (Raffel et al. 2007, 27-28)

4 LASERS AS LIGHT SOURCES

Lasers can emit monochromatic light with high energy thus making lasers optimal light sources for PIV systems. Light from laser can also be bundled into thin light sheets for illuminating tracer particles without chromatic aberrations. In general, lasers are composed out of three main components:

- The laser material
- The pump source
- The mirror arrangements.

The laser material consists of an atomic or molecular gas, semiconductor or solid material, the pump source excites the laser material by electromagnetic or chemical energy and the mirror arrangement, or resonator, allows an oscillation within the laser material. (Raffel et al. 2007, 28-29)

There are three elementary kinds of interactions that each atom can be brought into various energy states, i.e. spontaneous emission, absorption and stimulated emission. If an atom would have two hypothetical energy levels E_2 and E_1 where $E_2 > E_1$, spontaneous emission would occur so that an exited atom in energy level E_2 would drop down to energy level E_1 emitting a randomly directed photon with certain frequency and energy. The spontaneous emission can be described with equation (10):

$$E_2 - E_1 = h\nu, \tag{10}$$

where h is Planck's constant and ν is atom's frequency. The spontaneous emission occurs in very short but not exactly defined period of time. (Raffel et al. 2007, 29)

If a photon with appropriate frequency impinges an atom, two effects are possible. In the case of absorption a photon excites an atom from energy level E_1 to E_2 receiving the energy $h\nu$. In the case of stimulated emission the incident photon can stimulate an atom in the excited state E_2 into the state E_1 in a specific, non-spontaneous, transition

by emitting two photons. In addition to the incident photon, a second photon is emitted in phase with the former photon. All three reactions are presented graphically in the figure (14). (Raffel et al. 2007, 29)

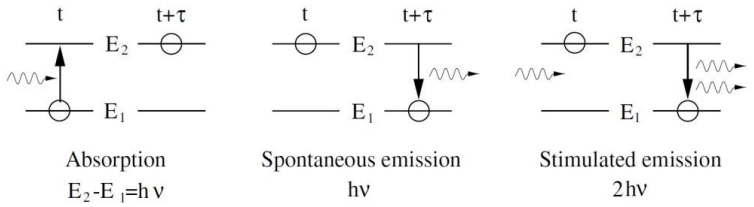

Figure 14. Elementary kinds of interactions between atoms and electromagnetic radiation (Raffel et al. 2007, 29)

When considering a large amount of atoms absorption and stimulated emission predominates. If the population of atoms in the energy level E_2 is marked as N_2 and the population in the energy level E_1 as N_1, in the case of $N_2 > N_1$ the stimulated emission predominates and in the case of $N_1 > N_2$ the absorption predominates. (Raffel et al. 2007, 30)

The basic principle of how laser works is based on the population inversion from N_1 to N_2, or vice versa, depending on the population density. By changing the energy states of the populations the needed photons to create laser are emitted. In normal conditions atoms exist at their ground state so external energy has to be transferred to the laser material to achieve population inversion. That can be done in multiple ways and the process is called pumping. Solid laser materials are pumped by electromagnetic radiation, semiconductor lasers by electric current and gas lasers by collision of the atoms or molecules with electrons or ions. (Raffel et al. 2007, 30)

The two energy levels are just for the theoretic perspective of how to produce laser. If only two energy levels are present, eventually the amount of atoms in each energy level will be the same, e.g. $N_1(E_1) = N_2(E_2)$. In average absorption and stimulated emission are as likely to happen so the material comes transparent at the frequency shown in equation (11):

$$\nu = \frac{E_2 - E_1}{h}, \tag{11}$$

thus no population inversion can be achieved anymore. For that reason at least three different energy levels of laser medium has to be introduced to achieve continuous population inversion and to produce laser. In three energy levels more than 50% of the atoms in the system have to be excited in order to amplify an impingement photon. The energy used for excitation is lost in the amplification process making the three energy level laser inefficient. When using four energy levels the lower laser level E_2 does not coincide with the basic level E_1 in room temperature keeping the basic level E_1 unoccupied. In this way achieving population inversion is easier and the four energy level laser requires less pumping power. The principles of three and four energy level lasers are presented in the figure (15). (Raffel et al. 2007, 30)

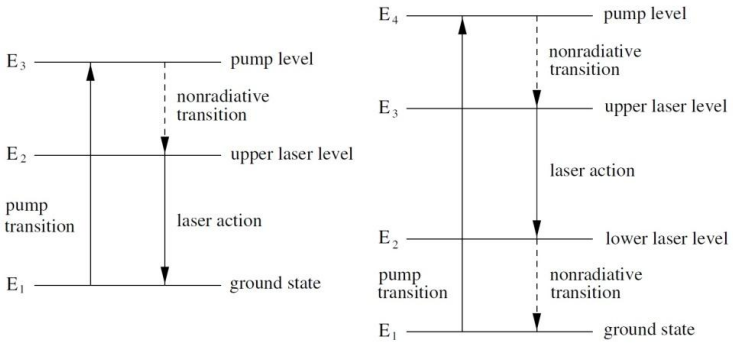

Figure 15. The principles of three and four energy level lasers (Raffel et al. 2007, 31)

In four level laser firstly the energy level E_4 is achieved by pumping the ground state with suitable frequency v which in this case is:

$$\nu = \frac{E_4 - E_1}{h}.$$

The upper laser level, E_3, is achieved with a rapid non-radiative transition. Metastable atoms in level E_3 stay there for a relatively long interim period of time before dropping down to lower laser level E_2 which is unoccupied. As shown in figure (15) the stimulated emissions to amplify the light occur between the energy levels E_3 and E_2 in four energy level laser. Simultaneously, spontaneous emission occurs in all directions causing excitation of further neighboring atoms which

initiates a rapid increase of stimulated emissions and therefore of radiation in a chain reaction. (Raffel et al. 2007, 30-31)

If the laser material is in cylindrical shape, the rapid increase of radiation occurs in a defined direction because the amplification is relative to the length of the laser medium. When the laser material is placed between two exactly aligned mirrors, i.e. optical resonator, the laser material forms an oscillator. Photons that are produced in the laser material reflect back from the mirrors amplifying the laser material again. This process is repeated many times and it generates photons which increase exponentially with the number of reflections finally resulting in a stationary process. In other words, standing waves are produced for a resonator length corresponding to the condition shown in equation (12):

$$L = \frac{m\lambda}{2n}, \tag{12}$$

where L is the length of the medium, n is the refractive index, m an integer number and λ is the wavelength. (Raffel et al. 2007, 30-31)

4.1 Popular lasers for PIV systems

There are many different laser types which can be utilized in PIV systems depending on their abilities and limitations. Different lasers vary mainly in the wavelength produced, the laser material and the pump source.

4.1.1 Helium-neon lasers

Helium-neon lasers, He-Ne lasers, are the most commonly used lasers. They are also the most effective ones in the visible range. The produced wavelength is 633 nm. Rather than illuminating the flow, He-Ne lasers are mostly used in the optical evaluation of photographic images. The laser transition, or laser action, takes place in

the neon atom. When an electrical discharge within the gaseous mixture of helium and neon occurs, the helium atoms are excited by the collision with the electrons. The main pump mechanism is when metastable helium atoms collide with neon atoms in the upper laser level. Commercial He-Ne lasers power is ranging from less than 1 mW to more than 10 mW. (Raffel et al. 2007, 32)

4.1.2 Copper-vapor lasers

Copper-vapor lasers, Cu lasers, are the most important neutral metal vapor lasers for PIV. The produced wavelengths are 510 nm and 578 nm and they are within yellow and green spectrum, respectively. The copper-vapor laser is an important pump source for dye lasers. In contrary to other laser types, Cu lasers need thermal insulation instead of cooling because the operating temperature can reach up to 1500 °C. Cu lasers are not for continuous operation due to the long life-span of the lower laser level. Repetition rates within the kHz-range can be achieved during pulse operations. The pulsed charge is burning between two electrodes which are located in the ends of a thermally insulated ceramic tube. Pressurized neon gas can be added as a buffer for improved performance. Cu lasers can achieve efficiency up to one percent. The Cu lasers are characterized by their high average power ranging from 1-30 W. (Raffel et al. 2007, 32-33)

4.1.3 Argon-ion lasers

Argon-ion lasers, Ar^+ lasers, are gas lasers similar to He-Ne lasers. The produced wavelengths are 514 nm and 488 nm. Typical for Ar^+ lasers are the need for very high currents needed to achieve for ionization and excitation of Argon atoms. The efficiency of Ar^+ lasers is around one tenth of a percent. In PIV Ar^+ lasers are usually used for low-speed water investigation. In blue-green range the power of Ar^+ lasers can be up to 100 W and near the ultraviolet range around 60 W. (Raffel et al. 2007, 33)

4.1.4 Ruby lasers

Ruby lasers, Cr^{3+} lasers, were the very first lasers ever introduced. The wavelength of the Cr^{3+} laser is 694 nm. Cr^{3+} use ruby crystal rods containing Cr^{3+} as an active medium so it is a solid-state laser. Cr^{3+} lasers are pumped optically by means of flash lamps. Cr^{3+} lasers are three level systems so suffer from poor efficiency as more than 50% of the atoms must be excited to obtain population inversion. For PIV Cr^{3+} lasers offer high pulse energies and its beam has good coherence. The disadvantage is that Cr^{3+} lasers light is in the edge of visible light spectrum and CCD cameras used in PIV are usually optimized for smaller wavelengths. (Raffel et al. 2007, 34)

4.1.5 Neodym-YAG lasers

For PIV the most important solid-state lasers are Neodym-YAG lasers, Nd:YAG lasers, which utilizes Nd^{3+} ion as the beam generator. For laser applications YAG crystals are commonly used but Nd^{3+} ion can be incorporated to different host materials as well. When using YAG crystals the laser has high amplification and good mechanical and thermal properties. Nd:YAG lasers' wavelength at standard operating temperature is 1064 nm and the excitation is achieved by optical pumping in broad energy bands and non-radiative transitions into the upper laser level. For tracer particle illumination purposes the original wavelength is frequency-doubled with crystals. By utilizing frequency-doubling the wavelength is transformed to 532 nm within the green spectrum. With frequency-doubling the second harmonic wave component of the original pump beam wave is separated with a nonlinear crystal also known as a second harmonic generator. The frequency-doubled light emerges with a polarization which is orthogonal to that of the original pump beam. The nonlinear crystal has to be oriented in such a way that the original pump beam is at right angle to the crystal's axis in order to achieve frequency-doubling. Around one third of the energy of the original source is transformed to the wavelength mentioned. (Raffel et al. 2007, 34-35, 40)

4.1.6 Neodym-YLF lasers

Another example of a laser utilizing Nd^{3+} ion is Neodym-YLF, Nd:YLF, laser. It produces light at the wavelength of 1053 nm and with frequency-doubling the light is transformed into visible range at 526 nm. Neodym-YLF lasers used in high-speed PIV techniques because its capability to produce reliable high average-power enabling efficient frequency conversion to visible wavelengths. (Raffel et al. 2007, 35)

5 LIGHT SHEET OPTICS

Light sheet optics is used for producing the light sheet for illuminating tracer particles. Different kind of lens configuration is used and sometimes needed to use to produce the desired light sheet profile. The most important single kind of lens for producing the light sheet is a cylindrical lens. The desired shape can be achieved with just one cylindrical lens if the laser beam diameter and divergence are small enough like with argon-ion lasers. For Nd:YAG lasers a combination of different lenses are needed to generate light sheet with proper thickness and intensity. (Raffel et al. 2007, 43)

When using a combination of different lenses, the first lens has to be diverging lens so that focal lines can be avoided. Also focal points have to be avoided with high power laser because the air in the vicinity of the focal point can be ionized. Focal lines do not usually ionize air but dust particles can be burnt in the vicinity. If air is ionized or dust particles are burnt, acoustic radiation occurs which affects the laser the beam properties. An example of lens configuration of light sheet optics is shown in figure 16: (Raffel et al. 2007, 44)

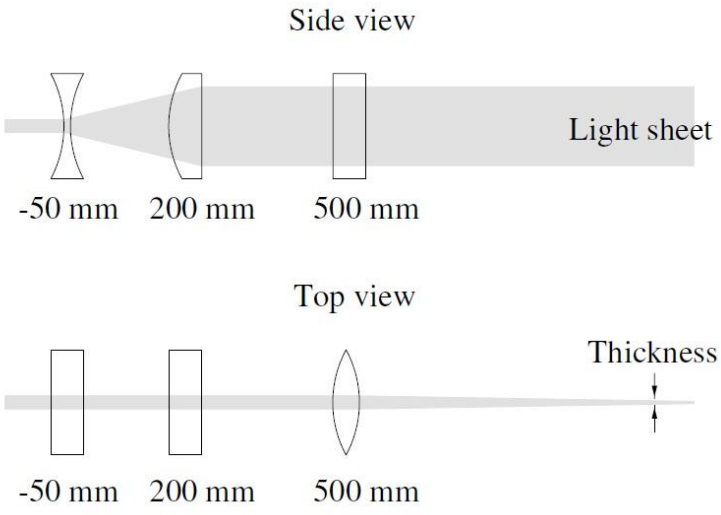

Figure 16. Light sheet optics using three cylindrical lenses (Raffel et al. 2007, 44)

The light sheet optics shown in figure 16 has three cylindrical lenses. The minimum thickness of the light sheet is a function of beam divergence of the laser and the focal length of the last cylindrical lens. For more versatile lens system, two telescopic lenses with a cylindrical lens can be used. An example of the system is presented in the figure 17: (Raffel et al. 2007, 44-45)

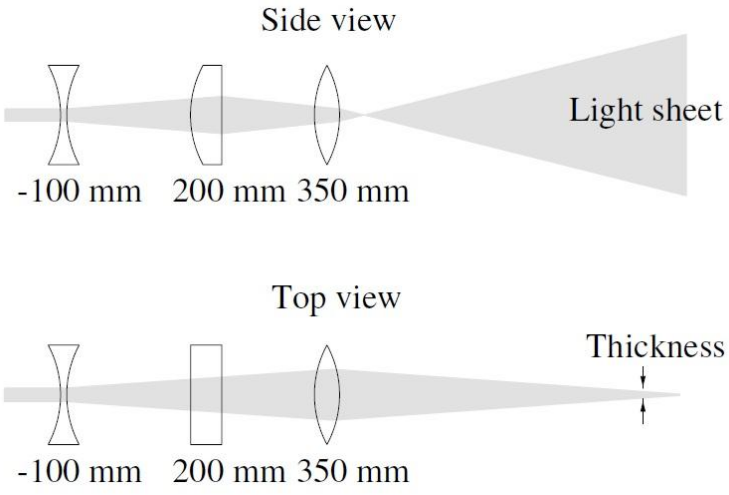

Figure 17. Light sheet optics with two spherical and one cylindrical lens (Raffel et al. 2007, 45)

The telescopic lenses are spherical in the figure 17. The height of the light sheet is function of the cylindrical lens' focal length in the middle. The thickness of the light

sheet is controlled by the spherical lenses. By shifting their positions respect to each other, the thickness of the light sheet can be adjusted. (Raffel et al. 2007, 44-46)

6 DIGITAL IMAGE RECORDING

Cameras are important part of the PIV system as they record the illuminated particles within the light sheet and enable the comparison of pictures. Like in normal use, digital recording is starting to replace old film cameras. The biggest advantage when using digital image recording is the immediate image availability and feedback of the recording. Also photochemical processing can be avoided by using digital image recording. Most commonly used devices are charged couple device, or CCD, and complementary metal oxide semiconductors, or CMOS. (Raffel et al. 2007, 69)

6.1 Technical description of CCD sensor

In nutshell, CCD sensor converts photons to electrons, in other words light to electric charge. The sensor consists of small elements called pixels. The size of a pixel is around 10x10 μm^2. A simplified model of a CCD sensor pixel and its operation mode is presented in figure 18: (Raffel et al. 2007, 69)

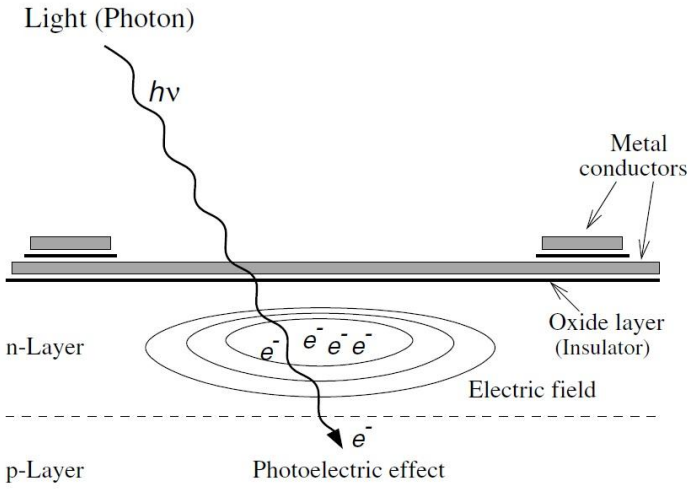

Figure 18. A CCD sensor (Raffel et al. 2007, 70)

A typical CCD sensor is built out of semiconducting substrate, like silicon, with metal conductors on the surface, an oxide layer as an insulator, an anode, referred as n-layer, and a cathode, referred as p-layer. (Raffel et al. 2007, 69-70)

A small voltage is applied between the metal conductors and the p-layer generates an electric field within the semiconductor. The local minimum in the electric field that is formed below the center of the pixel is associated with a lack of electrons and it is known as a potential well. The potential well allows charge, e.g. electrons, to be stored. When a photon of proper wavelength enters the p-n junction of the semiconductor, an electron-hole pair is generated. While the hole is absorbed in the p-layer, the generated electron migrates along the gradient of the electric field towards its minimum or potential well, where it is stored. Electrons continue to accumulate for the duration of the pixel's exposure to light. CCD sensors have typically full-well capacity between 10000 and 100000 electrons. If this number is exceeded during the exposure the extra electrons migrate to neighboring pixels. That leads to image blooming. Image blooming can be controlled with anti-blooming architectures in which overflowing charge is captured by conductors as it migrates toward the neighboring CCD cells. (Raffel et al. 2007, 69-71)

6.2 Technical description of CMOS sensor

As CCD sensors, CMOS sensor also converts light into electric charge and furthermore to an image. Their biggest difference to CCD sensors is that each pixel can individually be controlled. The main advantage of CMOS sensor is their high sensitivity and relatively low noise. A simplified model of CMOS sensor is presented in figure 19: (Raffel et al. 2007, 71)

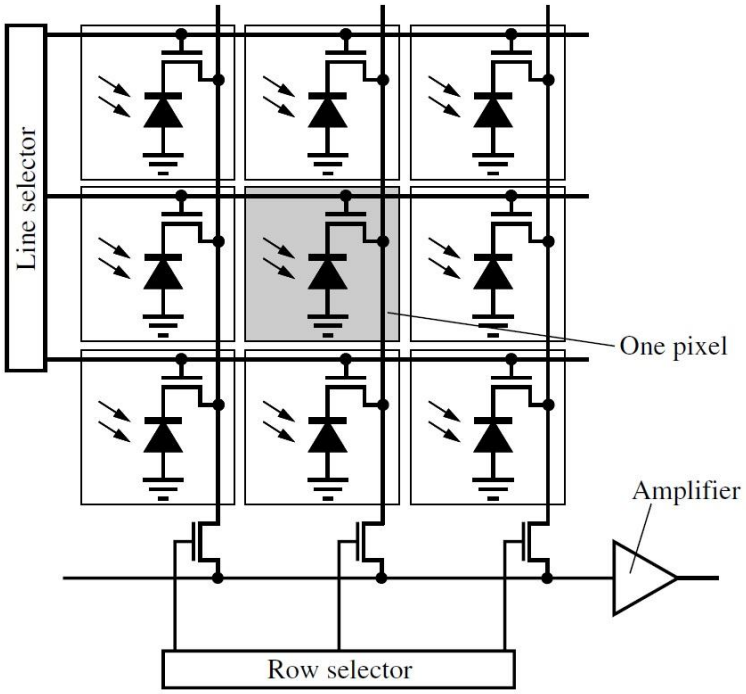

Figure 19. A CMOS sensor (Raffel et al. 2007, 71)

In CMOS sensor each individual pixel contains an electric circuit which is a big advantage. It allows integrating fundamental camera function like amplification, non-linear signal transformations and AD-conversion on chip. It also allows limiting the amount of active pixels in the sensor. Lower pixel count raises the framing rate. Downside of having an electronic circuit in every pixel is that the electric noise ratio increases. For PIV applications this means that larger CMOS sensors are not feasible to use. Electric noise ratio can be lowered by amplifying each pixel individually. (Raffel et al. 2007, 71-72)

6.3 Sources of noise in CCD and CMOS sensors

Electronic noise is present in both sensor technologies. Electric noise is always present when talking about any electrical machine. The biggest problem for imaging is the background noise level. That is due to the fact that the scattering efficiency of a tracer particle is too low and barely exceeds the background noise level. The bigger the observation area or larger the observation distance is, the harder it is to record an image of a scattering particle from the background noise level. (Raffel et al. 2007, 72)

The background noise is mainly due to the thermal effects in sensor. Thermal effects generate electron-hole pairs similarly as the ones that are generated by photoelectric effect. The current produced by temperature related electron-hole pairs is called dark current. Dark current distorts the picture and leads to situation where weak particles are hard to distinguish from noise. But as the production rate of temperature related electron-hole pairs is constant, the dark current can be accounted by subtracting a constant voltage at the output of the charge-to-voltage converter. One way also to diminish the effects of dark current is to use cooled sensors. Cryogenically cooled CCD sensors can produce less than one electron per second per each pixel. For every 6-7 °C increase in temperature the rate of generation of dark current doubles. (Raffel et al. 2007, 72)

Charge-to-voltage conversion during the readout sequence also produce noise referred to read noise or shot noise. Under normal operation typical CCD sensor generates noise level of several hundred electrons per each pixel for the period of integration (1/25 s or 1-30 s). By optimizing conversion electronics and by cooling this rate can be brought down to a level of few electrons per pixel. For normal PIV recording Peltier-cooled sensors are used nowadays. (Raffel et al. 2007, 72-73)

6.4 Comparison of CCD and CMOS cameras

Needless to say that the properties of digital cameras are important to obtain accurate results with image based measurement techniques, like PIV. Comparison of the sensor technologies is hard in the sense that the manufacturers rarely give out any detailed information about their sensors. Also generally accepted comparison standard does not exist. (Hain et al. 2007, 403-411)

A study made by Hain et al. in 2007 concluded the following:

- State-of-the-art CMOS cameras have good image quality. However, the image quality of the-state-of-the-art CCD cameras is still better. Thus, for high precision measurements a CCD camera should be applied.
- Intensified CMOS cameras further reduce the image quality and spatial resolution. However, their high sensitivities allow measurements at low illuminations with moderate signal-to-noise ratios, SNRs.
- For time resolved data acquisition, a CMOS camera without an intensifier is the best choice as long as the signal strength is acceptable.
- There is a strong difference between state-of-the-art imaging sensors.

Even with those conclusions it's hard to give any exact recommendation for a certain camera type. The requirement is strongly application related. Nevertheless, to capture high speed events CMOS camera must be used because of its high frame rate. (Hain et al. 2007, 403-411)

7 STATISTICAL AND MATHEMATICAL IMAGE EVALUATION

For analyzing of PIV images, a mathematical model of the recording and the statistical evaluation of PIV images must be performed. PIV recordings are evaluated

by locally cross-correlating two frames of single exposures of the tracer particles inside an interrogation area. In principle, the tracer particle ensemble inside the interrogation area is mathematically altered to one particle moving to a certain direction at certain speed.

7.1 Geometrical imaging

As mentioned before, PIV recordings are divided into interrogation areas. The geometrical back projection of those interrogation areas in the light sheet are referred as interrogation volumes. A measurement volume for statistical evaluation is defined by two interrogation volumes. Basic terms of geometrical imaging and the arrangement are presented in the figure 20. (Raffel et al. 2007, 80)

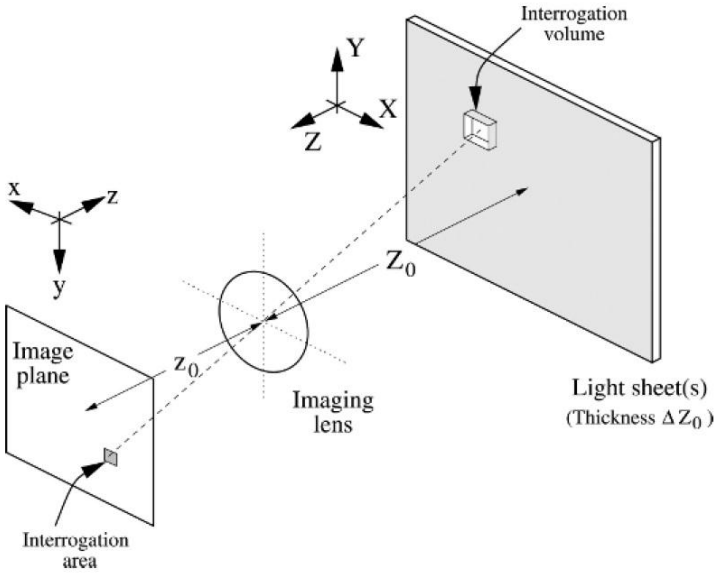

Figure 20. A schematic representation of geometrical imaging (Raffel et al. 2007, 80)

If the media is same on both sides of the lens, the focus criterion can be counted from equation 13:

$$\frac{1}{z_0} + \frac{1}{Z_0} = \frac{1}{f}, \tag{13}$$

where z_0 is the distance between the image plane and the lens, Z_0 is the distance between the lens and the object plane and f is the focal length of the imaging lens. The distances from the image plane to the lens and from the lens to object plane also defines the magnification factor, M: (Raffel et al. 2007, 49,79)

$$M = \frac{z_0}{Z_0} \ .$$

7.2 Locations of particle images in the object and the image plane

When considering a single exposure recording, it consists of random distribution of particle images. The mathematical description of the state of the tracer ensemble in three dimensional interrogation volume is presented in the equation 14:

$$\mathbf{\Gamma} = \begin{pmatrix} \mathbf{X_1} \\ \mathbf{X_2} \\ \vdots \\ \mathbf{X_N} \end{pmatrix}, \tag{14}$$

where $\mathbf{\Gamma}$ describes the state of the ensemble at any given time t, $\mathbf{X_i}$ is the position vector of the particle i at time t and N is the amount of tracer particles in the interrogation volume. The position vector $\mathbf{X_i}$ can be described as in equation (15):

$$\mathbf{X_i} = \begin{pmatrix} X_i \\ Y_\mathrm{i} \\ Z_\mathrm{i} \end{pmatrix} \ , \tag{15}$$

where X_i,Y_i and Z_i are the particle i coordinate positions.

In the interrogation area or image plane, the position vector can be mathematically described as in the equation 16:

$$\mathbf{x_i} = \begin{pmatrix} x_i \\ y_i \end{pmatrix} \ , \tag{16}$$

where $\mathbf{x_i}$ is the position vector for the particle i in the image plane and x_i and y_i are the particle's coordinate positions in the image plane. All coordinate positions in the object and image plane can be seen in the figure 20. (Raffel et al. 2007, 80)

The position vectors in the image and the object plane have relation presented in the equation 17:

$$\mathbf{X_i} = \frac{\mathbf{x_i}}{M} \text{ and } \mathbf{Y_i} = \frac{\mathbf{y_i}}{M} . \quad (17)$$

As the image plane is two dimensional the position vector for z-coordinate in the image plane does not exist. (Raffel et al. 2007, 80)

7.3 Intensity distribution in the image plane

The image can be best described with a point spread function by a convolution of the geometric image and the impulse response of the imaging system. The amplitude of the point spread function for infinite small particle and perfectly aberration-free, well focused lenses can be mathematically described by the square of the first order Bessel function also known as Airy function. In PIV systems the lenses do not fill the demand of being perfectly aberration-free. However, if the imaging lens' point spread function is assumed to be Gaussian versus x and y, which is common practice in the PIV literature, it can be mathematically described as in the equation 18:

$$\tau(\mathbf{x}) = Ke^{\left(-\frac{8|\mathbf{X}|^2}{d_\tau^2}\right)}, \quad (18)$$

where $\tau(\mathbf{x})$ is the point spread function of the imaging lens, d_t is the diameter of particle image which can be estimated from the equation 19:

$$d_\tau = \sqrt{\left(Md_p\right)^2 + d_{\text{diff}}^2} , \quad (19)$$

where d_{diff} is the diffraction limited minimum which can be obtained from equation 20:

$$d_{\text{diff}} = 2.44 \frac{f}{d_a}(M+1)\lambda , \quad (20)$$

where d_a is the aperture diameter. The coefficient K is described in the equation 21: (Raffel et al. 2007, 50, 81, appendix A.2)

$$K = \frac{8\tau_0}{\pi d_\tau^2}. \quad (20)$$

Schematically the situation is presented in the figure 21. (Raffel et al. 2007, 83)

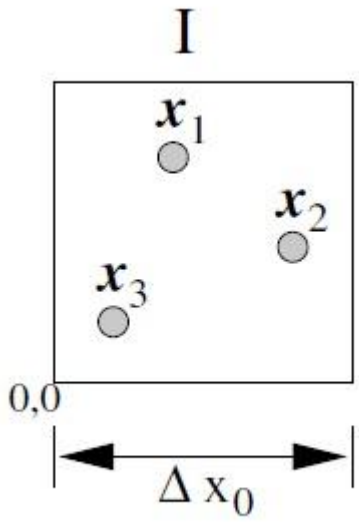

Figure 21. A schematic presentation of a single exposure image intensity field (Raffel et al. 2007, 83)

The image intensity field of the single exposure case can be expressed as in equation 21:

$$I = I(\mathbf{x}, \mathbf{\Gamma}) = \tau(\mathbf{x}) \sum_{i=1}^{N} V_0(\mathbf{X_i})\, \delta(\mathbf{x} - \mathbf{x_i}) \ , \quad (21)$$

where I is the image intensity field, $V_0(\mathbf{X}_i)$ is the transfer function giving the light energy of the image of an individual particle i inside the interrogation volume and δ is the Dirac delta-function describing the geometric part of the particle image.

The parameters affecting the visibility of the particle are its scattering properties, the light intensity at the particle position and the sensitivity of the recording optics and the sensor. However, it is assumed that the particles have the same scattering properties and recording optics and media have same sensitivity over the image plane. The image intensity in x- and y-coordinates in many situations is defined by adding weight kernels for different locations inside the interrogation area with weight

function. If it is assumed that the light intensity inside the interrogation volume is only function of Z and that it is the viewing direction and that the light intensity analyzed in X and Y depends only on the weight function, the transfer function can be written as in equation 22:

$$V_0(\mathbf{X}) = W_0(X,Y)I_0(Z)\,, \tag{22}$$

where $W_0(X,Y)$ is the interrogation window function backprojected into the light sheet and $I_0(Z)$ is the intensity profile of the light sheet. (Raffel et al. 2007, 81-82)

If it is assumed that the light sheet profile is Gaussian, the intensity profile of the light sheet can be written as in equation 23:

$$I_0(Z) = I_Z e^{\left(-8\frac{(Z-Z_0)^2}{\Delta Z_0^2}\right)}\,, \tag{23}$$

where I_Z is the maximum intensity of the light sheet and ΔZ_0 is the thickness of the light sheet and the extension of the interrogation volume in Z direction. (Raffel et al. 2007, 82)

Also if the window function is thought of being Gaussian, it can be written as in the equation 24:

$$W_0(X,Y) = W_{XY} e^{\left(-8\frac{(X-X_0)^2}{\Delta X_0^2} - 8\frac{(Y-Y_0)^2}{\Delta Y_0^2}\right)}\,, \tag{24}$$

where W_{XY} is the maximum value of the weight function at X_0 and Y_0 and ΔX_0 and ΔY_0 are the horizontal and vertical interrogation volume dimensions within the light sheet, respectively. Usually pulsed lasers do not have Gaussian intensity distribution and it is closer to a top-hat function. Also digitized recordings are usually interrogated in rectangular windows making the interrogation volume to be a rectangular box taking into consideration that interrogation volume dimensions are related to interrogation area dimension by the magnification factor. With those assumptions the intensity profile function of the light sheet can be written as in equation 25:

$$I_0(Z) = \begin{Bmatrix} I_Z \text{ if } |Z - Z_0| \leq \frac{\Delta Z_0}{2} \\ 0 \text{ elsewhere} \end{Bmatrix} \quad (25)$$

and the weight function as in equation 26:

$$W_0(X,Y) = \begin{Bmatrix} W_{XY} \text{ if } |X - X_0| \leq \frac{\Delta X_0}{2} \text{ and } |Y - Y_0| \leq \frac{\Delta Y_0}{2} \\ 0 \text{ elsewhere} \end{Bmatrix} . \quad (26)$$

With previous assumptions and with:

$$\tau(\mathbf{x} - \mathbf{x_i}) = \tau(\mathbf{x}) * \delta(\mathbf{x} - \mathbf{x_i}) \ ,$$

where * denotes convolution, the image intensity field in the equation 18 can be written as in equation 27: (Raffel et al. 2007, 81-83)

$$I(\mathbf{x}, \mathbf{\Gamma}) = \sum_{i=1}^{N} V_0(\mathbf{X_i})\, \tau(\mathbf{x} - \mathbf{x_i}) \ . \quad (27)$$

7.4 Mean value and autocorrelation of a single exposure recording

Quantities which are used for normalization of cross-correlation are the mean value and the variance of the image intensity field. The spatial average of image intensity field is presented in the equation 28:

$$\langle I(\mathbf{x}, \mathbf{\Gamma}) \rangle = \frac{1}{a_I} \int_{a_I} I(\mathbf{x}, \mathbf{\Gamma})\, \mathrm{d}\mathbf{x}, \quad (28)$$

where a_I is the interrogation area. (Raffel et al. 2007, 83)

The autocorrelation of the single exposure intensity field can be derived in the similar way from the equation 29:

$$R_I(\mathbf{s}, \mathbf{\Gamma}) = \langle I(\mathbf{x}, \mathbf{\Gamma}) I(\mathbf{x} + \mathbf{s}, \mathbf{\Gamma}) \rangle$$

$$= \frac{1}{a_I} \int_{a_I} \sum_{i=1}^{N} V_0(\mathbf{X_i})\, \tau(\mathbf{x} - \mathbf{x_i}) \sum_{j=1}^{N} V_0(\mathbf{X_j})\, \tau(\mathbf{x} - \mathbf{x_j} + \mathbf{s}) \mathrm{d}\mathbf{x} \ , \quad (29)$$

where $R_I(\mathbf{s},\mathbf{\Gamma})$ is the autocorrelation function and **s** is the separation vector in the correlation plane. (Raffel et al. 2007, 84)

The autocorrelation function can be decomposed into different terms as presented in the equation 30:

$$R_{\mathrm{I}}(\mathbf{s},\mathbf{\Gamma}) = R_{\mathrm{C}}(\mathbf{s},\mathbf{\Gamma}) + R_{\mathrm{F}}(\mathbf{s},\mathbf{\Gamma}) + R_{\mathrm{P}}(\mathbf{s},\mathbf{\Gamma}) \ , \qquad (30)$$

where R_C(**s,Γ**) is the convolution of the mean intensities, R_F(**s,Γ**) is the noise term due to the random particle correlations and R_P(**s,Γ**) is the particle image self-correlation peak located at position (0,0). A graphical representation of the autocorrelation function and its terms is presented in the figure 22. (Raffel et al. 2007, 84)

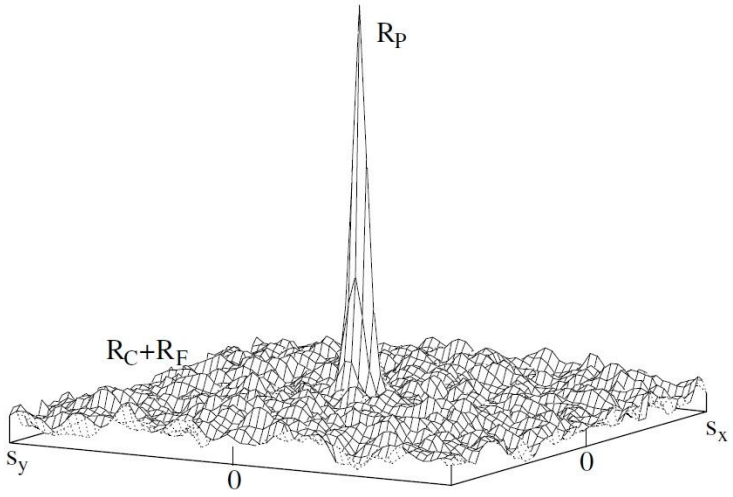

Figure 22. Autocorrelation function's terms presented graphically (Raffel et al. 2007, 85)

By distinguishing the $i \neq j$ terms which represent the correlation of different particle images and therefore randomly distributed noise in the correlation plane, and the i=j terms which represent the correlation of each particle image with itself, the equation 30 can be presented as in equation 31:

$$R_{\mathrm{I}}(\mathbf{s},\mathbf{\Gamma}) = \frac{1}{a_{\mathrm{I}}} \sum_{i \neq j}^{N} V_0(\mathbf{X_i}) V_0(\mathbf{X_j}) \int_{a_{\mathrm{I}}} \tau(\mathbf{x}-\mathbf{x_i})\, \tau(\mathbf{x}-\mathbf{x_j}+\mathbf{s}) \mathrm{d}\mathbf{x}$$

$$+ \frac{1}{a_{\mathrm{I}}} \sum_{i=j}^{N} V_0^2(\mathbf{X_i}) \int_{a_{\mathrm{I}}} \tau(\mathbf{x}-\mathbf{x_i})\, \tau(\mathbf{x}-\mathbf{x_j}+\mathbf{s}) \mathrm{d}\mathbf{x} \ . \qquad (31)$$

When considering the image intensity field given in figure 21, its schematic representation of the autocorrelation of the intensity field *I* is given in figure 23. (Raffel et al. 2007, 84-86)

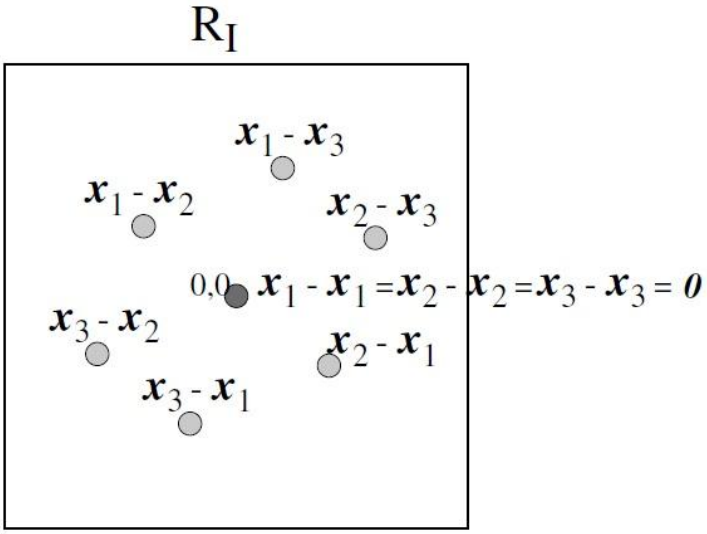

Figure 23. A schematic representation of autocorrelation of image intensity field (Raffel et al. 2007, 85)

The correlation peaks, R_F and R_P, occur at locations which are given by the vectorial differences between particle image locations. The strength of the peak is defined by the number of all possible differences in that location and thus the self-correlation peak, R_P, is the tallest peak. (Raffel et al. 2007, 84-86)

7.5 Cross-Correlating Two Singly Exposed Recordings

Previously the mathematical basis of PIV recording considering singly exposed recording was introduced. However, PIV recordings are most often evaluated by locally cross-correlating two frames of single exposures of the tracer ensemble. For that reason PIV system usually withholds two lasers for two consecutive illuminations of the tracer ensemble.

The displacement of the tracer ensemble assuming that the displacement is constant inside the interrogation volume during the second exposure at time t'=t+Δt is given in equation 32:

$$\mathbf{X_i'} = \mathbf{X_i} + \mathbf{D} = \begin{pmatrix} X_\mathrm{i} + D_\mathrm{x} \\ Y_\mathrm{i} + D_\mathrm{y} \\ Z_\mathrm{i} + D_\mathrm{z} \end{pmatrix}, \tag{32}$$

where $\mathbf{X_i'}$ is the particle position during the second exposure and **D** is the particle displacement within the flow field. For interrogation area the particle image displacements can be obtained from the equation 33:

$$\mathbf{d} = \begin{pmatrix} MD_\mathrm{x} \\ MD_\mathrm{y} \end{pmatrix}, \tag{33}$$

where **d** is the particle image displacement vector. By taking the displacement vectors into account the image intensity field for the second exposure is presented in the equation 34:

$$I'(\mathbf{x}, \mathbf{\Gamma}) = \sum_{j=1}^{N} V_0'(\mathbf{X_j} + \mathbf{D})\tau(\mathbf{x} - \mathbf{x_j} - \mathbf{d}), \tag{34}$$

where V_0' is the interrogation volume of the second exposure. If assuming identical light sheet and windowing functions, the cross-correlation function of the two interrogation areas is presented in the equation 35:

$$R_\mathrm{II}(\mathbf{s}, \mathbf{\Gamma}, \mathbf{D}) = \frac{1}{a_\mathrm{I}} \sum_{i,j} V_0(\mathbf{X_i}) V_0(\mathbf{X_j} + \mathbf{D}) \int_{a_\mathrm{I}} \tau(\mathbf{x} - \mathbf{x_i}) \tau(\mathbf{x} - \mathbf{x_j} + \mathbf{s} - \mathbf{d}) d\mathbf{x}, \tag{35}$$

where R_II is the cross-correlation function. And by distinguishing the noise terms, e.g. i≠j, and the terms that withhold the needed displacement information, eg. i=j, the cross-correlation function can be presented as in equation 36:

$$R_\mathrm{II}(\mathbf{s}, \mathbf{\Gamma}, \mathbf{D}) = \frac{1}{a_\mathrm{I}} \sum_{i \neq j} V_0(\mathbf{X_i}) V_0(\mathbf{X_j} + \mathbf{D}) \int_{a_\mathrm{I}} \tau(\mathbf{x} - \mathbf{x_i}) \tau(\mathbf{x} - \mathbf{x_j} + \mathbf{s} - \mathbf{d}) d\mathbf{x} + \frac{1}{a_\mathrm{I}} \sum_{i=j} V_0(\mathbf{X_i}) V_0(\mathbf{X_i} + \mathbf{D}) \int_{a_\mathrm{I}} \tau(\mathbf{x} - \mathbf{x_i}) \tau(\mathbf{x} - \mathbf{x_j} + \mathbf{s} - \mathbf{d}) d\mathbf{x}. \tag{36}$$

As for single exposure recording, the correlation of two singly exposed recordings can be decomposed into three different parts presented in equation 37:

$$R_\mathrm{II}(\mathbf{s}, \mathbf{\Gamma}, \mathbf{D}) = R_\mathrm{C}(\mathbf{s}, \mathbf{\Gamma}, \mathbf{D}) + R_\mathrm{F}(\mathbf{s}, \mathbf{\Gamma}, \mathbf{D}) + R_\mathrm{D}(\mathbf{s}, \mathbf{\Gamma}, \mathbf{D}), \tag{37}$$

where R_D represents the component of the cross-correlation function that corresponds to the correlation of images of particles obtained from the first exposure with images of identical particles obtained from the second exposure, e.g. *i=j* terms. A graphical representation of the cross-correlation function and its terms is presented in figure 24. (Raffel et al. 2007, 86-88)

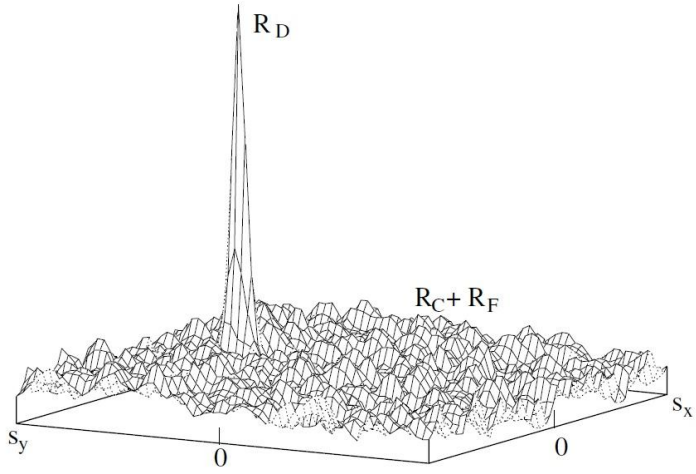

Figure 24. Terms of cross-correlation function presented graphically (Raffel et al. 2007, 87)

If the image intensity fields recorded at time *t* and *t*' (*t*'=*t*+Δ*t*) are as presented schematically in figure 25. (Raffel et al. 2007, 86-88)

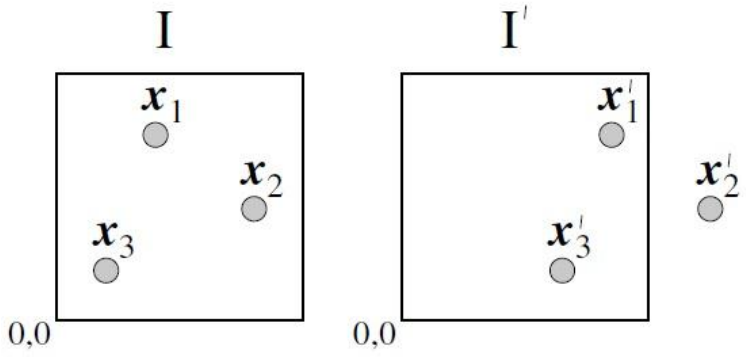

Figure 25. Intensity fields of two singly exposed images (Raffel et al. 2007, 87)

The cross-correlation of the image intensity fields I and I' can be schematically represented as in figure 26. (Raffel et al. 2007, 86-88)

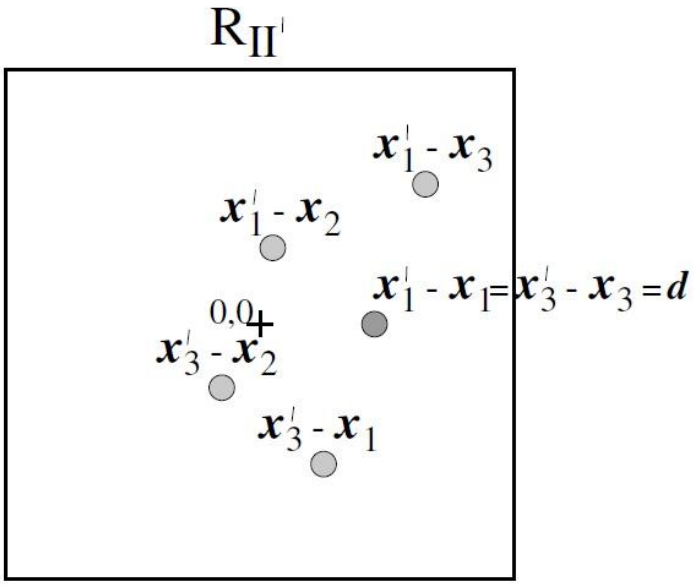

Figure 26. A schematic representation of cross-correlation of image intensity fields (Raffel et al. 2007, 88)

The x_2' is missing from the figure 26 because it is located outside the interrogation window as shown in the figure 25. (Raffel et al. 2007, 86-88)

8 DESCRIPTIONS OF APPLICATIONS UTILIZING PIV SYSTEM

The PIV measuring system is acquired mainly for the use of Nuclear Safety Research Unit in LUT. The Nuclear Safety Research Unit will be utilizing the PIV system in its PPOOLEX test facility for steam blowdown experiments. As PIV system is offering great possibilities for flow field studies, the Department of Fluid Dynamics in LUT will be also utilizing the PIV system for its centrifugal compressor test station, CCTS. The Laboratory of Thermodynamics in LUT has no actual laboratory equipment but utilization of the PIV system is taken into consideration in the future if any new laboratory equipment is built or acquired.

8.1 PPOOLEX

PPOOLEX, designed and constructed in 2006 by Nuclear Safety Research Unit in LUT, is modeling the dry and wet well compartments of a suppression pool of BWR containment. The PPOOLEX facility consists of a wet well compartment known as condensation pool, dry well compartment, inlet plenum and air/steam line piping. The dry and wet well compartments are separated by an intermediate floor. A route for gas/steam flow from dry compartment to wet compartment is created with a vertical blowdown pipe or pipes attached underneath the floor. The test vessel which is the main component of the facility is 7.45 meters in height and 2.4 meters in diameter. The total volume of the vessel is around 31 m^3. The vessel is constructed with three plate cylinder segments and with dome sections in both ends. Both the dry and wet well is volumetrically scaled according to the compartment volumes of the Olkiluoto NPPs containments in ratio approximately 1:320. The injection of gas in question is done through the side wall of the dry compartment. A schematic illustration of the air and steam line piping is shown in figure 27. (Laine et al. 2011, 7-9)

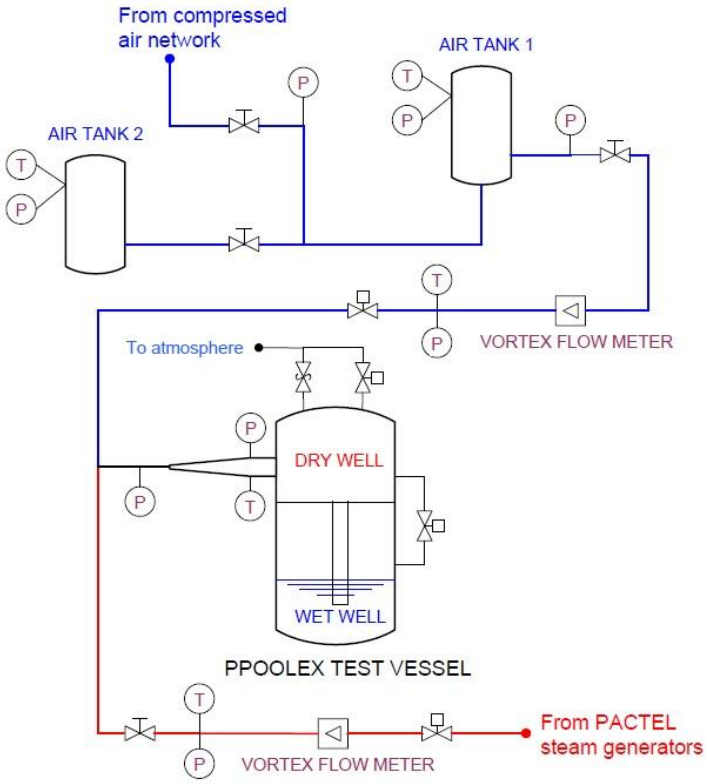

Figure 27. Arrangement of air and steam supply in PPOOLEX facility (Laine et al. 2011, 9)

Steam needed in the experiments is produced in PACTEL test facility. Steam is generated by heating its 1 MW core section and with its three horizontal steam generators. The generated steam is led to the dry well through insulated steam line made of sections of standard DN80 and DN50 pipes. For stratification experiments a short Ø18x1.5 bypass section in parallel to the DN50 line. For non-condensable gas injection laboratory's compressed air network with its air accumulators is used. The vessel has several windows for visual observation in both compartments. The bottom of the vessel has a drain pipe with a manual valve (DN100). A relief valve is located in the removable vessel head. The bottom dome section is also removable and has a man hole (DN500) in it. The test vessel is shown in figure 28. (Laine et al. 2011, 7-9)

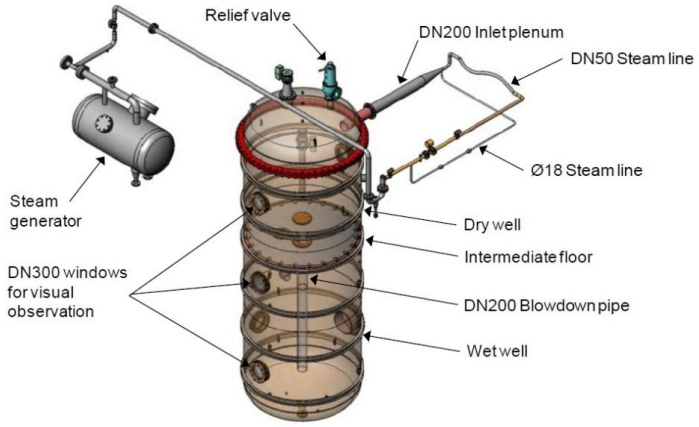

Figure 28. PPOOLEX test vessel (Laine et al. 2011, 8)

The blowdown pipe (DN200) is inside the wet well and located 300 mm off the centre of the condensation pool. (Laine et al. 2011, 7-9)

8.2 Centrifugal compressor test station

One of the applications where PIV measuring system is utilized is the CCTS shown in figure 29. (Turunen-Saaresti Teemu 2004, 61-65)

Figure 29. Centrifugal compressor test station (Turunen-Saaresti Teemu 2004, 61)

The CCTS consists of a centrifugal compressor, a suction section before the compressor inlet and a blow out section after the compressor outlet. (Turunen-Saaresti Teemu 2004, 61-65)

Air enters the test station through a mass flow nozzle, throttling valve A and a flow straightener. The compressor is driven directly by a high speed electric motor. The electric motor can be run accurately by controlling the electric current with an inverter. As the electric motor is directly installed to the compressor shaft there is no gear box in the test station, e.g. it utilizes a single shaft construction. The compressor

is completely oil-free due to the use of magnetic bearings. The compressor has seven full and seven splitter blades with 40° back lean from the radial direction. After the compressor the air exits the blow out section through a valve B which is a throttling valve. The compressor's pressure ratio is 1.94 at the design point. The layout of the test station is shown in figure 30. The centrifugal compressor test station is part of the Laboratory of Fluid Dynamics. (Turunen-Saaresti Teemu 2004, 61-65)

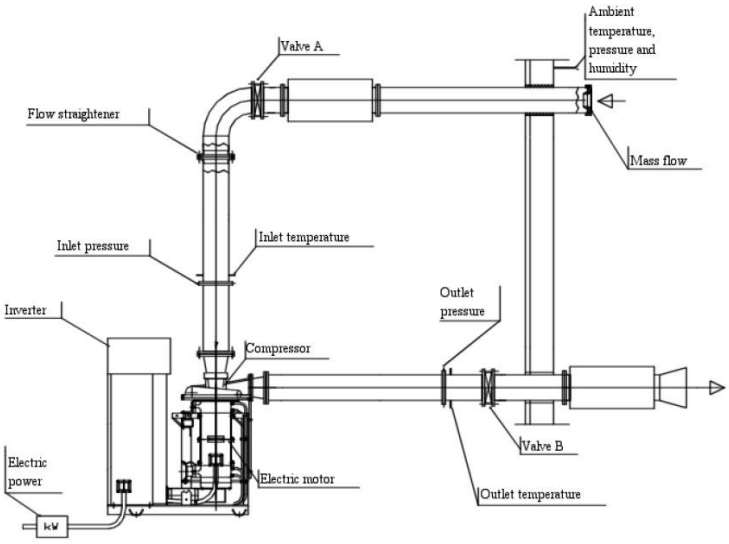

Figure 30. The layout of the centrifugal compressor test station (Turunen-Saaresti Teemu 2004, 64)

9 ACQUIRED PIV SYSTEM

After the procurement process the winning tender was submitted by LaVisionUK Ltd. The acquired PIV system allows measurements in both of the applications it was designed for, the PPOOLEX and the CCTS. For the further applications the PIV system can be completed with extra system parts if needed.

9.1 Laser

The system's laser is Nd:YAG double-cavity laser. The laser has a telescopic resonator and it fulfills laser CLASS4 requirements according to standard EN60825-10:2001-11. The two pulsed Nd:YAG lasers are mounted on a single baseplate. The

lasers emit the beam in infrared range at 1064 nm and they are polarization combined. A second harmonic generator is used to convert the beam to visible range at 532 nm. Dichroic mirrors separate the visible light from the residual infrared light and direct the beam to the experiment. The delay between two pulses can be controlled with external trigger source. The specification of the lasers is presented in the table 3. (LaVision IV 2009)

Table 3. Performance values of lasers used in the acquired PIV system (Lavision IV 2009)

Laser charasteristics	**Performance value**
Beam diameter	6.35 mm
Pulse width	7-9 ns
Energy stability	±2% RMS
Energy @ 532 nm	180 mJ
Repetition rate	0-15 Hz
Divergence, full angle for 90% of output energy	< 0.8 mrad
Beam pointing stability	< 100 μrad
M^2 value	≈ 3.5
Power supply	1x650 W

9.2 Laser accessories

All mounts for supporting the double-cavity laser are included. For the compressor measurements a laser endoscope with tube length of 200 mm and tube diameter of 8 mm is included. Laser endoscope has divergence angle of circa 60°. (LaVision I 2007)

9.3 Light sheet optics

System's light sheet optics uses a combination of two spherical lenses and one cylindrical divergence lens. The arrangement of lenses and the generation of the light sheet are presented in the figure 31. (LaVision V 2011)

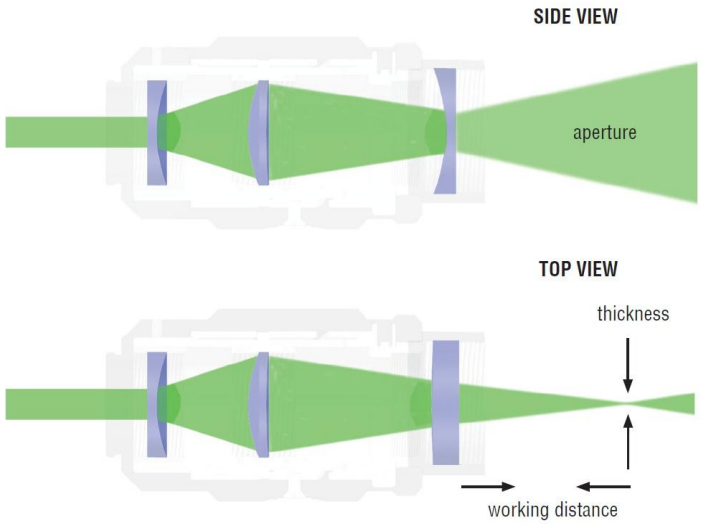

Figure 31. Light sheet optics arrangement of the PIV system (LaVision V 2011)

The appropriate thickness of the light sheet is achieved with the two spherical lenses. The thickness of the light sheet can be controlled by the separation of the two spherical lenses. The aperture and the height of the light sheet are controlled by the focal length of the divergence lens and the diameter of the laser. The height of the light sheet can be adapted by changing the divergence lens. The lens material is BK7 which is widely used in the field of optics. The system's light sheet optics has three different divergent lenses with focal length of -10 mm, -20 mm and -50 mm. The working distance is from 300 mm to 2000 mm. (LaVision V 2011)

9.4 Cameras

The chosen cameras needed to have a capability of working with endoscopes for compressor application. As there was no need for utilizing system in high speed

applications and in that sense there was no need for CMOS cameras. The system's cameras are Imager Pro X 4M CCD camera. The camera type has progressive-scan technology with dual frame-technique for cross correlation. The CCD sensors are cooled with Peltier element to +10°C. The camera utilizes partial scan meaning that at reduced region of interest the frame rate can be elevated. Other specifications of Imager Pro X 4M camera are presented in the table 4. (LaVision III 2009)

Table 4. General system specifications of Imager Pro X 4M CCD camera (LaVision III 2009, LaVision VII 2011)

Camera charasteristics	**Performance value**
Double shutter	two images with 115 ns min. interframing time
Dynamic range A/D	14 bit
Number of pixels	2048x2048 pixels
Pixel size	7.4 x 7.4 μm^2
Frame rate	14 frames/s
Camera memory	4 GB
Spectral range	290-1100 nm
Maximum quantum efficiency	yield point 55% at 500 nm
Full well capacity	40000 e-
Size of the camera head	84x66x175 mm^3

9.5 Camera accessories

For faster use a Camera Link is included in the system. The Camera Link allows faster download of the taken images and they are transferable to a system computer in real time. Camera Link cables are also included. With remote controlled focus rings the focus and aperture of the camera lenses can be controlled with computer software. Depending on the lens where the remote controlled focus ring is used, the focus can be adjusted in more than 106 steps and the aperture in more than 105 steps. The system has also a remote controlled Scheimpflug mount which allows all areas of the image plane to be in focus. Scheimpflug mount is used in stereo-PIV imaging. The remote controlled focus ring can be used with the Scheimpflug mount or

independently. Lenses for cameras are 50 mm in focal length and the maximum aperture is 1.4. Lenses are used with the remote focus ring. For endoscope use a lens with 85 mm focal length is included. For stereo PIV without endoscope use two lenses with 105 mm in focal length and with luminous intensity of 2.8 are included. With all lenses two camera filters with 532 nm wavelength and 10 nm bandwidth can be used. (LaVision I 2007)

For endoscope use a camera endoscope with tube length of 200 mm and tube diameter of 10 mm is included in the system. Endoscope's viewing angle is 65° and direction of view is 0° in forward direction. Beam can be steered 90°. An example of endoscope arrangement is presented in the figure 32. (LaVision I 2007)

Figure 32. An example of endoscope arrangements for laser and camera (LaVision I 2007)

For 3D PIV measurement, a 2x2 plane calibration plate in size of 300 mm x 300 mm is included. (LaVision I 2007)

9.6 System computer and software

For collecting PIV recording and other data the system has a system computer. The system computer is part of the PIV system whereas data analyzing can be done in separate computers. The main specifications of the system computer are presented in the table 5. (Boaler 2011, LaVision I 2007)

Table 5. Main specifications of the system computer (Boaler 2011, Lavision I 2007, LaVision VII 2011)

Feature	Specification
Processor type	2x Intel Xeon X5650
Processor clock rate	2.66 GHz
Processor cores	6
Processor cache memory	12 MB
RAM memory type	DDR3 1333MHz
RAM memory	12 GB (6x2 GB)
Hard disk type	4x Seagate Constellation ES 7200.1
Hard disk memory	2 TB (4x500 GB)
Hard disk speed	7200 rpm
SAS RAID system type	2x Western Digital 1TB SATA RAID1

As mentioned before, the further analyzing of PIV recording data can be done in separate computers. The system includes three separate “floating” style analysis licenses meaning that analyzing can be done in any three computers at the same time. For speeding up analyzing, system includes three graphics processing units that utilize parallel data processing. Graphics processing units speed up the PIV calculation by factor of ten or more. (Boaler 2011, LaVision I 2007)

The system utilizes DaVis software solution for image acquisition and analysis of flow fields in both 2D and 3D cases. DaVis software is written in a fully integrated macro programming language (CL) which is similar in syntax to C++. It allows modifying and adding capabilities of the DaVis software. User can also create

completely new macros and add unique and customized functions to the software. DaVis software supports following file types: bmp, jpg, tif, dat, txt and PostScript. DaVis software also supports data interface to LabView, MathCAD, Matlab, Techplot and common CFD softwares. (Boaler 2011, LaVision I 2007)

9.7 Seeding

For seeding of gas flow an aerosol generator with 4 atomizer nozzles is included. The generator has inlet for pressurized air and the seeding density can be controlled with pressure controller. The counter pressure of the generator is up to 10 bars of counter pressure. (LaVision VII 2007)

10 POSITIONING PIV SYSTEM INTO PPOOLEX

The main purpose for using PIV for PPOOLEX is to obtain information about the collapsing of bubbles due to condensation during blowdown experiments. Test results will be used for validating CFD data obtained with computer simulations. The positioning of the system is important to obtain the best possible data from the measurements. The ultimate goal when positioning the PIV system is to achieve the best possible lighting conditions. For obtaining the out-of-plane vector component the position arrangement is done with two cameras.

10.1 Positioning of CCD cameras

As example Mie diagrams show, in figures 3 to 7, when using two cameras, the same scattering intensity can be achieved by positioning cameras in 90° to each other in the different sides of the light sheet. In that sense the positioning of cameras can be

done in straightforward manner by building camera inlets in 90° compared to each other.

10.2 Positioning of laser for stereo-PIV

The laser can be positioned in three different ways in relation to cameras for stereo-PIV measurement. The first option is to shoot the laser towards the cameras so that the meeting angle for a camera and the laser is 135°. This kind of arrangement is also called forward-forward-scattering arrangement. The second option is to shoot the laser behind the cameras so that the meeting angle for a camera and the laser is 45°. This kind of arrangement is called backward-backward-scattering arrangement. Cameras would be on the different sides of the light sheet. The third option is to shoot the laser behind the cameras so that the cameras are on the same side of the light sheet. The meeting angle for laser and a camera 1 is 45° and 135° for camera 2. This arrangement is called forward-backward-scattering arrangement. The downside of the third option is that the scattering intensities are not equal for both cameras and depending on the measuring conditions the intensity for the camera recording the backward-scattering might not be strong enough. And on the other hand the intensity for the camera recording forward-scattering can be too strong and the sensor can break.

10.3 Limitations and things to consider

The biggest limitation for fully free positioning of the system is that the PPOOLEX condensation pool is on one side close to a wall of the laboratory. The gap between the wall and the PPOOLEX is too narrow for both the laser and the cameras. There are also horizontal welds in the PPOOLEX that somewhat limit the positioning vertically as there have to a minimum distance between two welds.

There are three possible places for the blowdown pipe of the PPOOLEX to be mounted in. When taking into consideration that there is not enough space for the laser of cameras to be mounted between the PPOOLEX and the wall, only one option of the possible three blowdown pipe positions can be taken into consideration.

During the blowdown experiments, PPOOLEX moves vertically which has to be taken into consideration when planning new observation windows for PPOOLEX for PIV use. In other words the size of a window needs to large enough to compensate the vertical movements. The vertical movements are in the millimeter range so it is not a too restricting limitation but still needs to be taken into consideration.

There are also existing observation windows in the PPOOLEX that can be utilized for laser and cameras but they are vertically too high from the exit of the blowdown pipe. It is more feasible to record with cameras from below the blowdown pipe since then the blowdown pipe itself will not be blocking the view for the cameras.

10.4 The final positioning plan

Taking limiting factors into consideration and to obtain the best possible scattering intensities, the positioning of the PIV system to PPOOLEX is shown in figure 33.

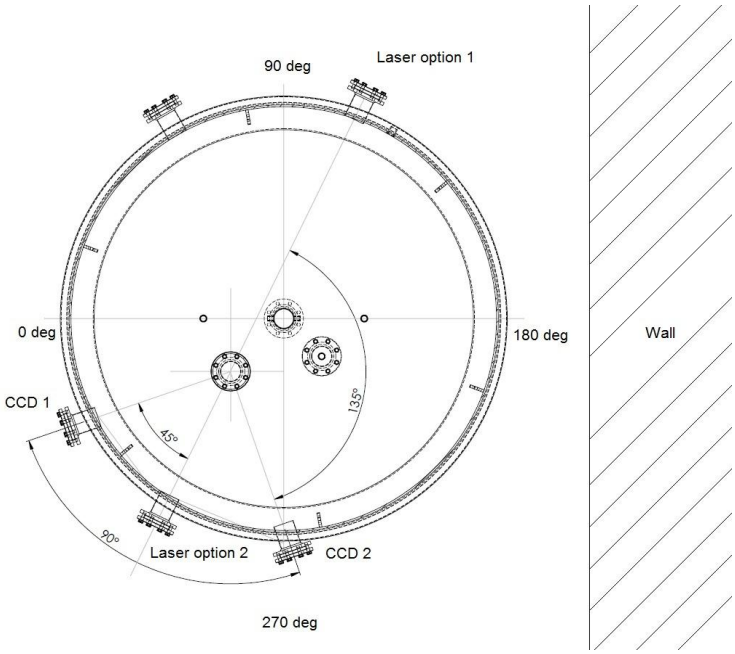

Figure 33. The positioning of the PIV system to PPOOLEX

The location of the blowdown pipe is firstly moved to the sector between 270° and 0°. The laser option 1 in the figure 33 is the optimal position because of the forward-forward-scattering arrangement. The cameras are positioned 135° to the laser sheet and the cameras are on the different sides of the laser sheet. To obtain backward-backward scattering the laser can be positioned in the laser option 2. Depending on the amount of gas bubbles inside the tank the distance for laser option 1 can be too much because light scatters from the bubbles. In that case laser option 2 can also come into consideration even though it offers inferior lightning conditions.

If conditions for stereo-PIV will be too challenging to obtain good data, 2D-PIV measurement can be done by using CCD1 and CCD2 inlets. Then laser can be positioned either to CCD1 or CCD2 inlets and camera 1 to the one that is left out. Used laser and camera options for respective measurement types are assembled to the table 6.

Table 6. Different measurement arrangements for PPOOLEX experiments.

Measurement type	Camera 1	Camera 2	Laser
Forward-forward-scattering stereo-PIV	CCD1	CCD2	Laser option 1
Backward-backward-scattering stereo-PIV	CCD1	CCD2	Laser option 2
2D-PIV	CCD1/CCD2	-	CCD2/CCD1

11 LASER SAFETY

Laser safety is very important when operating PIV system because the system utilizes a high-powered laser for illuminating the measured flow. Without a careful use of the laser, the beam can cause serious damage to eyes or skin. Limits that should not be exceeded for eye or skin exposures are defined by the International Electrical Commission's, IEC's, standard IEC 60825-1 which is the base for regional standards for EU (EN 60825-1) and Finland (SFS EN 60825-1).

11.1 Injuries caused by lasers

In principle laser beam can hit on every surface of the human body and thus cause an injury. Laser beams are monochromatic, coherent, the diameters of the beam s are usually really small and the radiance is huge causing the energy of the beam to focus in a really small volume where the threshold value of the tissue can be easily exceeded. The sensitivities of different tissues do not differ much from each other. The relevant factors considering the possible tissue damage are the amount of absorbed energy and the wave length of the laser. (Pastila et al. 2009, 77)

Due to the optical and anatomical characters of eyes, they are the most vulnerable to laser radiation between 400 nm to 1400 nm. Between those wave lengths optical radiation can be transmitted from the cornea to the retina. The anatomical structure of an eye where cornea and retina can be located is presented in the figure 34.

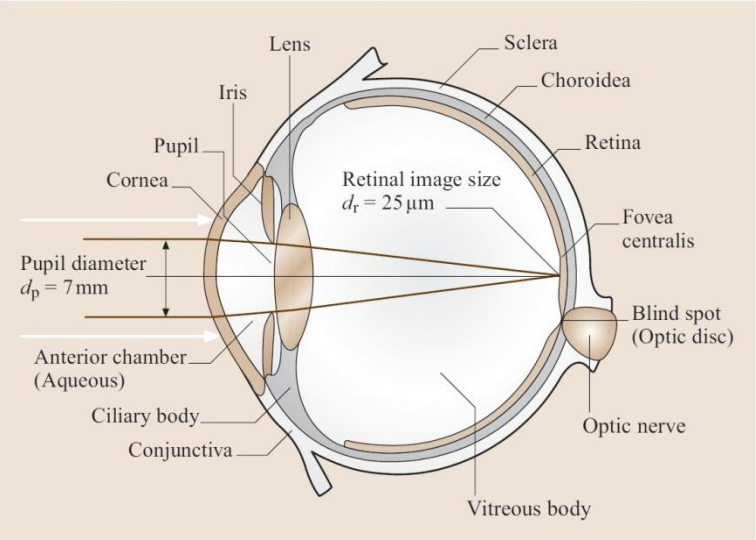

Figure 34. An anatomical structure of an eye (Träger et al. 2007, 1253)

The most fundamental interaction between the laser light and the tissue is absorption. The energy carried by the photons transforms into other kinds of energy, mostly to excitation of atoms and vibration of molecules. The excitation and vibration increases the heat content of the tissue. The interaction of laser radiation with biological tissue can be described as a function of the irradiance, *E*, given in units W/m^2 or radiant exposure, *H*, in J/m^2.

Irradiances up to 1 W/cm^2 normally result in reversible processes such as photostimulation or photochemical reactions in the skin if exposure times are longer than 1 s. At higher irradiances from 10 W/cm^2 to 10^5W/cm2 in the time regime from few milliseconds up to few seconds the biological tissue becomes heated. The heating of biological tissue can result in cell necrosis because of coagulation of proteins. If temperature is elevated above 100 °C, vaporization of cell substances such as water occurs. At even higher irradiances up to 10^{10} W/cm^2 and exposure

durations of microseconds, so called nonthermal effects are initiated. Nonthermal effects result in the ablation of superficial layers of the tissue caused by mechanical disruption. If even higher irradiances and shorter exposure durations can occur so called optical breakdown happens. In optical breakdown the electrical field amplitudes exceed the atomic or intramolecular Coulomb wall and therefore microplasma is created resulting in ionizing effect. The rapid expansion of this plasma causes a shockwave which have a capability to destroy even hardest substances in human body. The main effects of laser radiation on biological tissue are presented in table 7 with respective exposure times and irradiances. The main effects of laser radiation as a function of wavelength in the eye and skin are presented in the table 8.

Table 7. The effects of laser radiation on biological tissue (Träger et al. 2007, 1257)

Photochemical effect	Photothermal effect	Photoionizing effect
Biostimulation	Hyperthermia	Ablation
	Coagulation	Disruption
	Carbonization	Fragmentation
	Vaporization	
t = 10-1000 s	t = 10 ms-1 s	t = 10 ps-10 µ
≤50 mW/cm2	1-100 W/cm2	

Table 8. Effects of laser radiation in eye and skin as function of wavelength region (Träger et al. 2007, 1257)

Wavelenght region	Eye	Skin
400-700	Photochemical and photothermal damage to the retina	Photosensitive reaction and skin burns (reddening of skin, blisters, charring)
700-1400	Cataract formation from heating proteins in the lens and photothermal damage to the retina	Skin burns (reddening of skin, blisters, charring, damage to underlying organs)

11.2 Maximum Permissible Exposure

For safety considerations and protection from laser radiation Maximum Permissible Exposure, MPE, values have been established. In normal circumstances, the MPEs represent the level of laser radiation that a person can be exposed to without suffering from adverse effects. The MPEs are defined separately to eye and skin. The MPEs are derived from animal testing and because of the fact that the MPEs are extrapolated to human tissue some uncertainties exists. But there are safety factors included in the MPEs that should cover uncertainties of that and of the procedure how they are defined. As strict values for humans with biological differences are hard to define, the MPEs should be used for guidelines in control of exposure and the exposure for laser radiation should be kept as low as possible. (Träger et al. 1260-1262)

MPEs for eye and skin exposure can be defined from the IEC's standard IEC 60825-1. There are predefined MPE values for eye and skin that are function of the exposure time for a single pulse. The single exposure MPE values in respective of system's laser values is for the eye 5 mJ/m^2 and for the skin 200 mJ/m^2. The values are defined from the IEC 60825-1 standard's tables A.1 and A.3.

11.3 Nominal Ocular Hazard Distance

The safety distance or Nominal Ocular Hazard Distance, NOHD, for the laser beam can be estimated with the equation (38):

$$\mathrm{NOHD} = \frac{1}{\varphi}\sqrt{\frac{4P_0}{\pi E_{\mathrm{MPE}}}} - \frac{a}{\varphi}, \tag{38}$$

where NOHD is the Nominal Ocular Hazard Distance, φ is the divergence of the laser beam, P_0 is the optical power of the laser, E_{MPE} is the respective MPE value (for eye) and a the diameter of the beam (Pastila et al. 2009, 46).

As the NOHD is in the kilometer range for class 4 lasers the use of laser safety goggles is advisable. The optical density of the laser safety goggles can be defined from the equation (39):

$$D_\lambda = \log \frac{E_0}{E_{\mathrm{MPE}}}, \tag{39}$$

where D is the optical density in respective wavelength λ, E_0 is the exposure value for incoming beam and E_{MPE} is the MPE value of the eye. (Pastila et al. 2009, 108)

The optical density of the laser safety goggles respective to maximum pulse power of the system's laser is 5.97. In the figure 35 is shown the NOHDs and optical densities for different laser power.

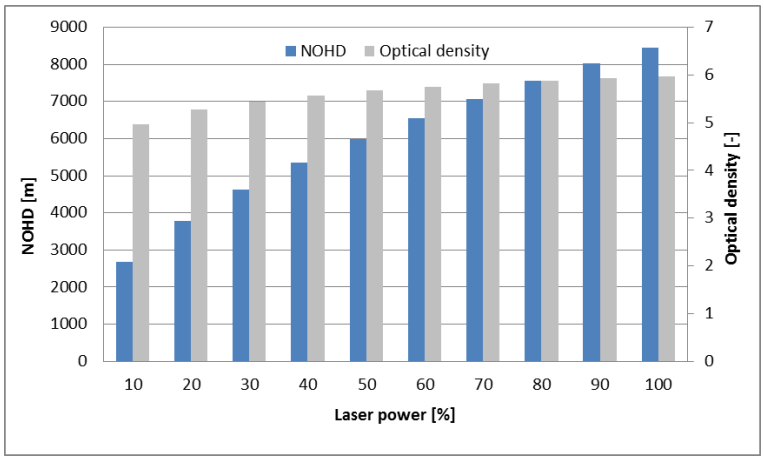

Figure 35. NOHDs and optical densities for different laser power

11.4 Exposure values for system's laser

When measuring or calculating exposure values an appropriate aperture should be used. The limiting aperture is defined in terms of the diameter of a circular area over which irradiance or radiant exposure is averaged. For eye and skin different limiting apertures exist. In the range of 400 nm to 1400 nm limiting aperture for eye is 7 mm and for skin 3.5 mm. (IEC 2007, 60)

Limiting apertures, respective diameters and exposure values for eye and skin of system's laser with maximum pulse energy is presented in table 9.

Table 9. Exposure values for laser with maximum pulse energy

Value	Eye	Skin
Limiting aperture [mm]	7	3,5
Aperture's diameter [m^2]	$3.848 \cdot 10^{-5}$	$9.621 \cdot 10^{-6}$
Exposure value [J/m^2]	4677.2	18708.8

The peak power of the laser pulse can be defined from the equation (40):

$$P_{\text{peak}} = \frac{E}{t}, \tag{40}$$

where P_{peak} is the peak power, E is the energy of the pulse and t is the duration of the pulse (Wilson J. & Hawkes J. 1998, 257).

The average power of the laser can be defined from the equation (41):

$$P_{\text{ave}} = Ef, \tag{41}$$

where P_{ave} is the average power of the laser and f is the frequency of the laser or repetation rate (Pastila et al. 2009, 297).

The power values at maximum pulse energy, the minimum duration of the pulse and the maximum repetition rate are presented in the table 10.

Table 10. Power values for system's laser

P_{peak} [MW]	P_{ave} [W]
25.7	2.7

11.5 Protective measures when using laser

The main principles of safe use of laser are that the beam never should be aimed towards a person, the laser should be used in a controlled environment, the laser should be stored and kept properly and the components that affect the beam path are installed steadily. The protective measures for different laser classes are presented in the table 11. (Pastila et al. 2009, 104-105)

Table 11. Protective measures when using laser (Pastila et al. 2009, 105)

Laser class	Protective measure
Class 1M	Preventing of looking straight into the beam with an optical aid
Class 2	Ending of the beam path
	Controlling of the beam path
Class 2M	Labeling of boundaries and passageways in the facility
	Removal of unnecessary reflections
Class 3R	Preventing of looking straight into the beam
Class 3B	Safety locks on the doors of the facility
	Removal of keys from laser when it is not used
	Protection of eyes
Class 4	Protection of skin

11.6 Possible hazardous situations when using laser

In an article by Träger et al. in 2007 were listed reasons for hazardous situations and common unsafe practices that are causes of preventable laser accidents:

- High retinal irradiance results when the beam is focused by the lens of the eye to create an extremely high retinal risk for visible and near-infrared lasers.
- Low beam divergence resulting in a large intrabeam hazard distance.
- Not wearing protective eyewear in the laser control area.
- Available eye protection not used.
- Wearing the wrong eyewear.
- Misaligned optics and upwardly directed beams.
- Equipment malfunction.
- Improper methods of handling high voltage.
- Intentional exposure of unprotected personnel.
- Bypassing of interlocks, door and laser housing.
- Insertion of reflective materials into beam paths.
- Lack of pre-planning.
- Turning on power supply accidentally.
- Operating unfamiliar equipment.
- Lack of protection from non-beam hazards.
- High irradiance at the focal point of an external lens creating greater skin hazard risk. (Träger et al. 2007, 1274)

11.6 Measures taken to guarantee laser safety in the PPOOLEX laboratory facility

There were many measures executed for the PPOOLEX laboratory facility to guarantee the safe use of laser during the experiments. The main goal was to ensure that no laser light can escape out from the PPOOLEX facility. This was executed by ordering custom-made covers for all observation windows made out of dimout blanket. The observation windows are fully covered with them and no laser light can escape through them. Whenever the laser is operated all operators must wear laser safety goggles. The optical density of the safety goggles is high enough to stop the laser beam from damaging the eye. Anyone operating the laser is advised to wear

safety goggles. Announcement before opening the shutter or operating the laser should be stated in a manner that everyone can hear.

All entrances to the laboratory are locked whenever using laser prohibiting persons not participating in the experiment from entering the laboratory facility accidentally. All entrances are marked properly with necessary warning signs. There is also a blinking red light outside the main entrance indicating that an experiment is in process and a sign saying that entrance is prohibited when the light is on.

Anyone operating the laser is instructed beforehand about the possible hazards considering the laser use and about all the safe measures that should be taken into consideration. Also there has to be at least two persons present when operating laser for possible emergency cases. All safety measures will be marked in the Nuclear Research Safety Unit's quality manual.

12 PIV EXPERIMENT IN PPOOLEX

The experimental part of the thesis was conducted in PPOOLEX facility in December of 2011. The functionality of the PIV system was tested beforehand using a smaller scale test facility. Used tracer particles were also tested in the smaller scale test facility before applying them to PPOOLEX. Used tracer particles were recommended by the supplier for this application. The main objective of the experiment was to obtain possible validation data for CFD and to obtain information about the functioning of the experimental setup and measuring parameters such as the amount of seeding material and correct time delay between laser pulses. The blowdown steam was generated in PACTEL facility.

12.1 Experimental setup

The arrangement of cameras and the laser were done in forward-forward-scattering manner as shown in figure 33 and in the table 6 to obtain stereo-PIV. The calibration

plate was mounted with a special device to the exit of the blowdown pipe. A laser pointer was used to get the calibration plate into the correct place paraller to the laser windows. After installing of the calibration plate the PPOOLEX was filled with water so that the actual calibration could be performed. The calibration images for cameras 1 and 2 are presented in the figure 36 and 37.

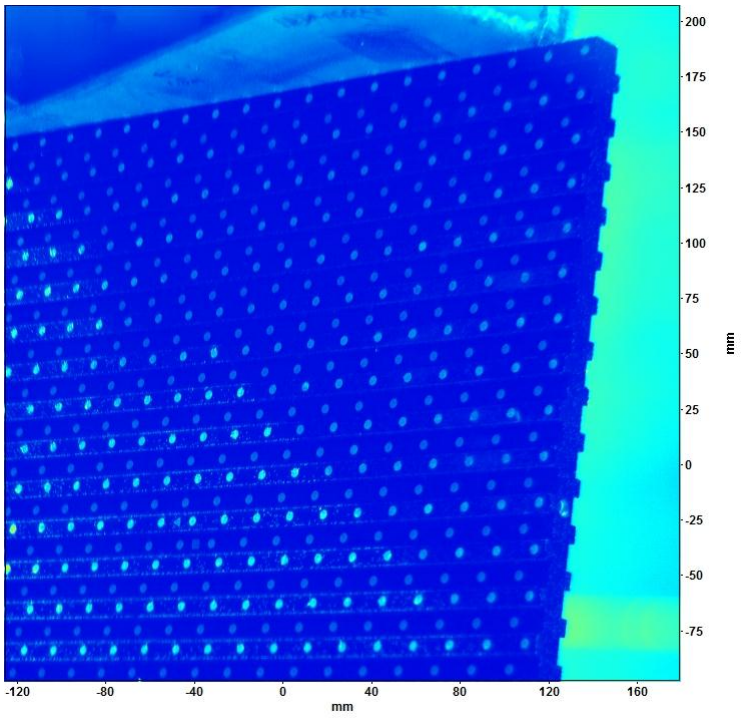

Figure 36. The calibration image of the camera 1

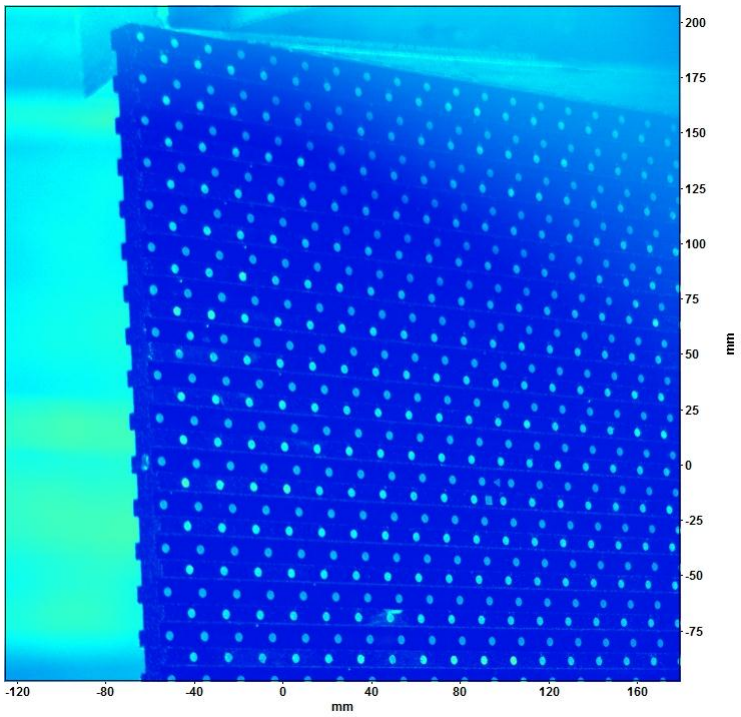

Figure 37. The calibration image of the camera 2

In the calibration images can be seen the exit of the blowdown pipe and the mounting device (top left corner in figure 36 and top right corner in figure 37). To achieve good focus across the calibration plate the scheimpflug angle was changed for both cameras. The focal distance to object plane for camera 2 was changed after achieving the best possible focus throughout the plane to match the one for camera 1. It was achieved by adding the width of the calibration plate to the focal distance thus the distances to object plane were at the same level. Maximum apertures were applied to keep the depth of field as small as possible. For the seeding glass hollow spheres were used. The amount of seeding was evaluated beforehand and mixed into the water in PPOOLEX. A small reduction to the correct amount of the seeding was done because of possible impurities contained in the water that might act as tracers. Homogenous distribution was achieved by blowing steam into PPOOLEX which mixed the water before the actual experiment. It was thought to be the most convenient way to obtain the homogenous distribution. For the generation of the laser light sheet a divergence lens with a focal length of -0.50 mm was used. The laser sheet alignment was done both before and after the filling of the PPOOLEX with water. The pulse delay was varying from 30000 µs to 60000 µs because the

flow velocities are very low. The optimal pulse delay was achieved with trial and error technique varying it between the values mentioned before. Important parameters of the experiments are presented in the table 12.

Table 12. Important parameters of the experiments

Parameter	Value
Seeding particles	Glass hollow spheres
Mean diameter of the seeding particles [µm]	11
Amount of seeding [g]	2
Density of seeding material [g/cm^3]	1.10
Amount on water in PPOOLEX before steam blowdown [m^3]	~ 9
Laser sheet thickness [mm]	7
FOV [mm x mm x mm]	300x300x7
Frequency between image pairs [Hz]	5
Time delay between laser pulses [µs]	30000-65000
Image pairs for one camera per measurement [-]	1000
Focal length of lenses [mm]	50
Scheimpflug angle for camera 1 [°]	2.6
Scheimpflug angle for camera 2 [°]	-2.5

12.2 Image preprocessing

The role of the image preprocessing is to improve the quality of the raw images before the actual PIV processing where in plane and out of plane vectors are obtained. The main image preprocessing applied to raw images were applying a geometrical mask on the pictures and subtracting sliding minimum over time. The unedited background raw images are presented in figures 38 and 39.

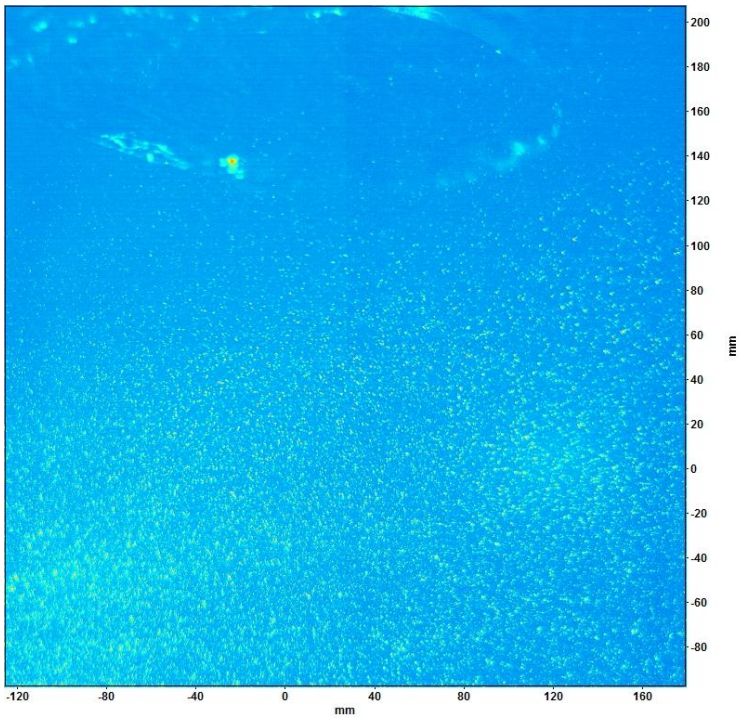

Figure 38. A background raw image with seeding for camera 1

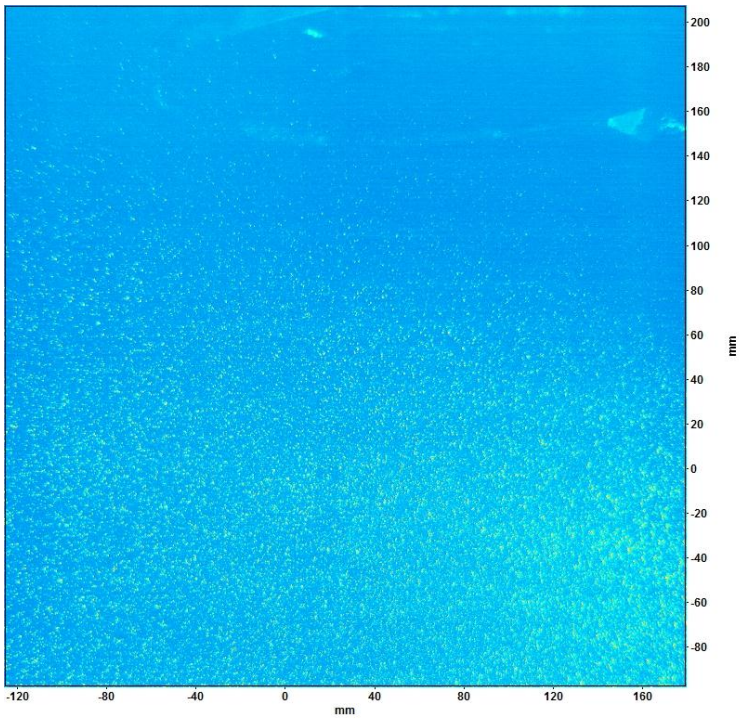

Figure 39. A background raw image with seeding for camera 2

From the unedited raw images can be seen that the outer edge of the blowdown pipe cause little reflection which is not profitable for the PIV processing. It also can be seen that the seeding density is more unified and in general better in lower parts of the FOV.

12.2.1 Geometrical masking

In some occasions a need for masking out some parts of the raw image is necessary. For example, there can be high reflection from a shiny surface that can affect the PIV processing. Also there can be some areas which have poor quality of correlation peaks which need to be masked out. With geometrical mask an area which will be masked out can be drawn on the raw image and then applied to every raw image so that the same area is always masked out. For both cameras' raw pictures individual geometrical mask must be applied as they are facing the measurement area in different angles. The geometrical masks applied to camera 1 and camera 2 raw images are shown in figures 40 and 41.

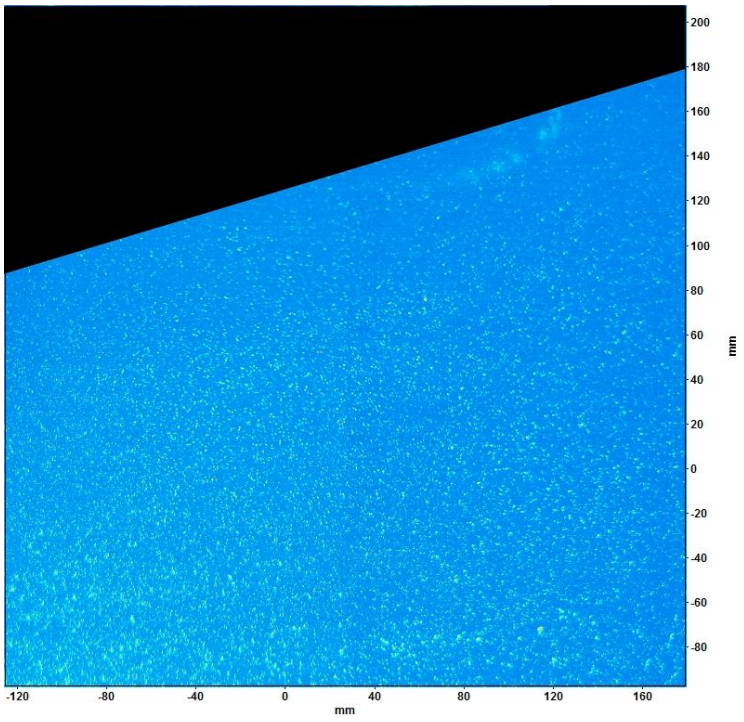

Figure 40. Geometrical mask applied for raw images of camera 1

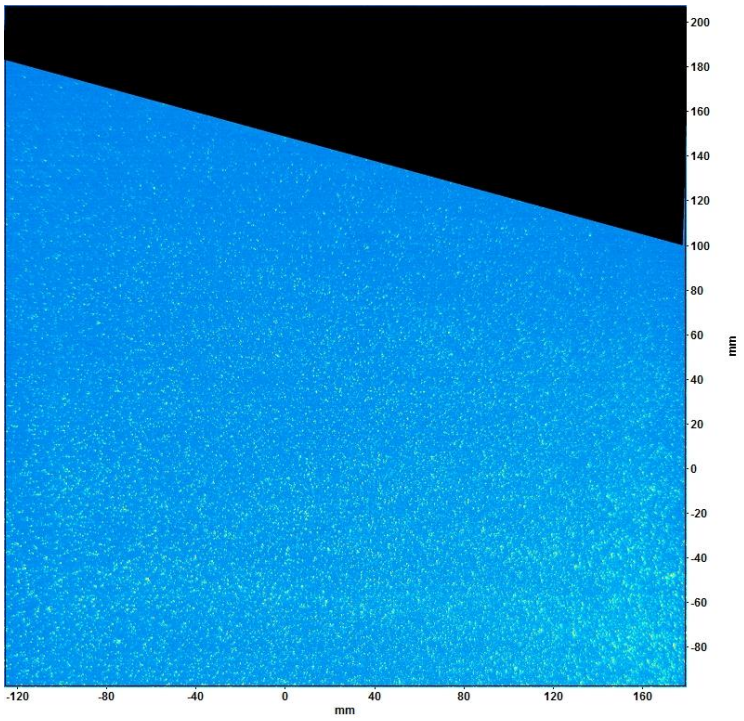

Figure 41. Geometrical mask applied for raw images of camera 2

The initial intent was to mask out only the blowdown pipe area as it does not withhold any important velocity information. But it was found out that the areas in vicinity of the exit of the blowdown pipe had bad quality of correlation peaks and the velocity information was not reliable. The probable cause for this was the lack of seeding material in the vicinity of the exit of the blowdown pipe. The blowdown steam does not have any tracer particles and as it condenses in the exit of the blowdown pipe the seeding density decreases.

12.2.2 Subtracting sliding minimum over time

The minimum intensity from 3 consecutive images was counted and then the average minimum intensity was subtracted from current source image thus making the quality of the raw images better. The filter also extracts all the constant intensities between the image sequence. An example of a raw image after applying subtract sliding minimum over time filter is presented in figure 42.

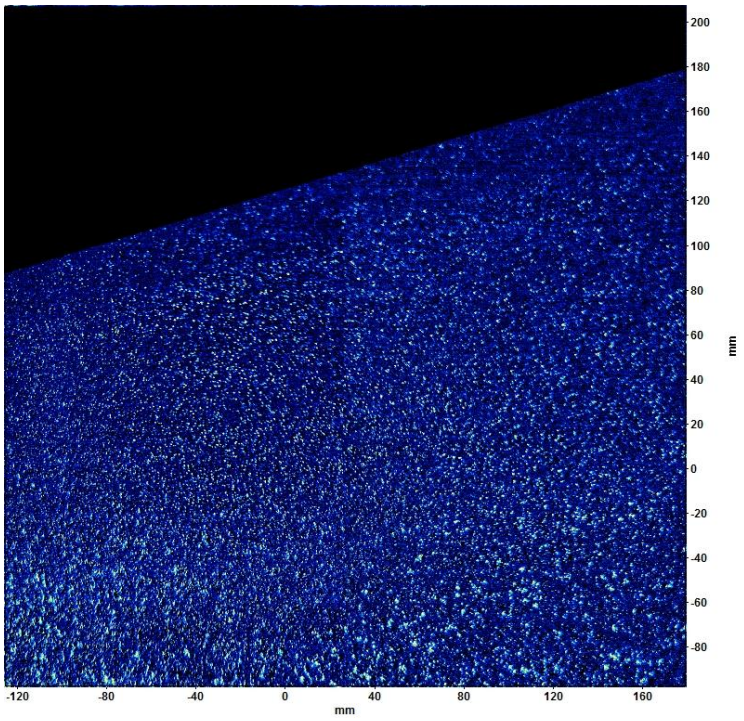

Figure 42. An example of a raw image of camera 1 after applying subtract sliding minimum over time filter on it

12.3 Results

The results presented in this thesis are of one of the measurements of the series of measurements performed. The measurement series included 8 independent measurements with changing values in the pulse delay and in the mass flow of blowdown steam. The objective was to achieve a steam-water interface in the exit of the pipe. The reason was firstly to avoid excessive amount of steam bubbles to enter the FOV and secondly to investigate if the flow around the blowdown pipe is constant in any way. The steam mass flow was controlled with an adjustable valve and kept at the same setting throughout the measurement. The optimal pulse delay was chosen with trial and error technique as there was little velocity information previously available. The main parameters for the PIV system for the measurement in question are presented in table 13.

Table 13. The main parameters for PIV system

Parameter	Value
Scheimpflug angle for camera 1 [°]	2.6
Scheimpflug angle for camera 2 [°]	-2.5
Distance to object plane for camera 1 [m]	1.040
Distance to object plane for camera 2 [m]	0.943
Aperture of camera 1	1.4
Aperture of camera 2	1.4
Laser pulse energy for laser 1 [%] / [mJ]	52/93.6
Laser pulse energy for laser 2 [%] / [mJ]	45/81
Time delay between pulses [µs]	65000

The main parameters for the PPOOLEX system for the measurement in question is presented in table 14.

Table 14. The main parameters for PPOOLEX system

Parameter	Value
Temperature of the blowdown steam [°C]	121.2
Pressure of the blowdown steam [bar]	~2.1
The volume flow rate of the blowdown steam [l/s]	23.3
Temperature of the pool water [°C]	19.1
Valve setting for the adjustive valve from PACTEL to PPOOLEX [%]	33

With the parameters presented in tables 13 and 14 the best condition to obtain the steam-water interface in the pipe exit without sudden bursts of steam bubbles was achieved.

In the measurement it was found out that there is fluctuation in the velocity field when the steam-water interface was situated in the exit of the pipe. There was found three different stages that had similarity in their velocity fields. It indicates that the condensation of steam in the vicinity of the pipe exit causes these fluctuations. For a strong constant outflow was usually followed a strong constant inflow towards the pipe exit. In between the two phases the movement of the velocity field was rather constant and the movement was towards the outer edge from the centerline of the pipe exit. In this middle phase the velocities were relatively small compared to the stronger outflow and inflow phases. There was no external triggering involved during the measurement of the vector fields. Recognizing of similar phases was done manually. Similar phases were picked out from the whole series of velocity field images for averaging purposes. If the whole series of vector field images would have been averaged the stronger outflows would have smoothen the stronger inflows out and vice versa. By extracting vector field images corresponding the correct phase averaging was achievable. The series of 1000 vector field images were analyzed for the results. The majority of the velocity field images were hard to categorize as the velocities were either too small or there was no continuous pattern of the velocity field, only an indication that the flow was towards the exit of the blowdown pipe in the vicinity of it. In areas underneath the vicinity of the exit of the blowdown pipe the flow direction was in general from the right hand side towards the left hand side. In addition to a stronger outflow and inflow periods and the period between them there was also indication that swirls beneath the exit of the blowdown pipe were formed. The swirls were clockwise in direction and appeared in similar positions in the measurement.

12.3.1 Average vector field of the stronger outflow phase

The set of 85 velocity field images were characterized by relatively strong outflow from the pipe exit from the set of 1000 velocity field images analyzed in total. The average velocity field is presented in the figure 43.

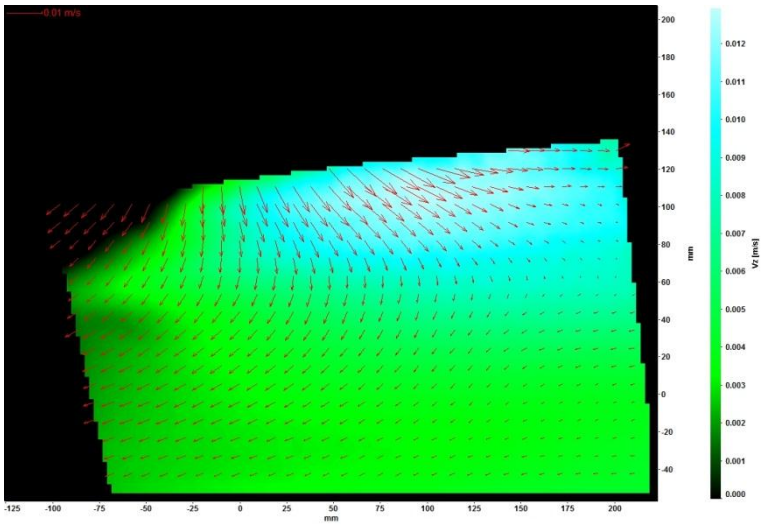

Figure 43. The averaged velocity field of the strong outflow phase

The reference vector with a value of 0.01 m/s is shown in the top left corner of the figure 43. The background color refers to the out of plane velocity component and the scale is in the right side of the figure 43. In the figure 43 the average velocities vary roughly from 0.01 m/s to 0.001 m/s. A larger version of the figure 43 is presented in the appendix I in the figure 1. The velocity field images can also be presented with background image of the cameras. The background image is comprised of the images from camera 1 and 2 and also represents the combined object plane for stereo-PIV. The averaged velocity field with background image is presented in the figure 44.

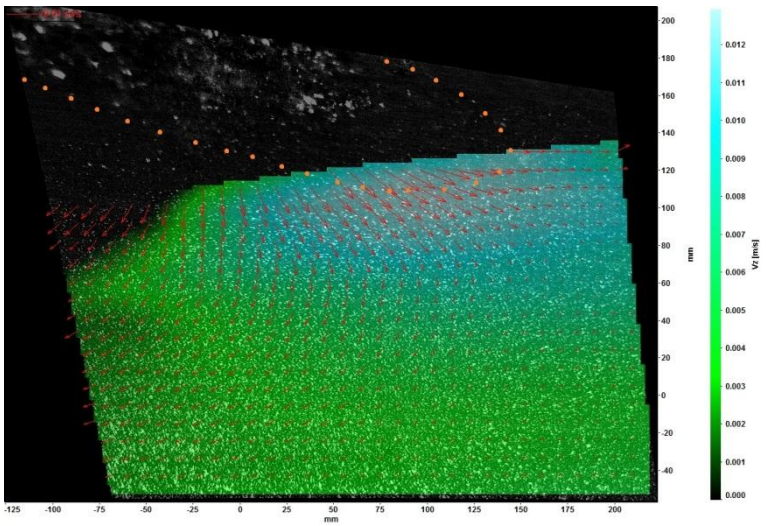

Figure 44. The averaged velocity field of the strong outflow phase with background image

In the figure 44 the outline of the pipe's exit is highlighted with orange dots. Due to the geometrical masking some velocity information is lost in the top left corner below the pipe exit as well as in the top right corner next to the pipe wall. The time intervals between the same phases were alternating from 0.2 seconds to 3.2 seconds. The maximum length of the stronger outflow phase was 0.8 seconds.

12.3.2 Average vector field of the stronger inflow phase

The set of 114 velocity field images were characterized by relatively strong inflow to the pipe exit. The average velocity vector field is presented in the figure 45.

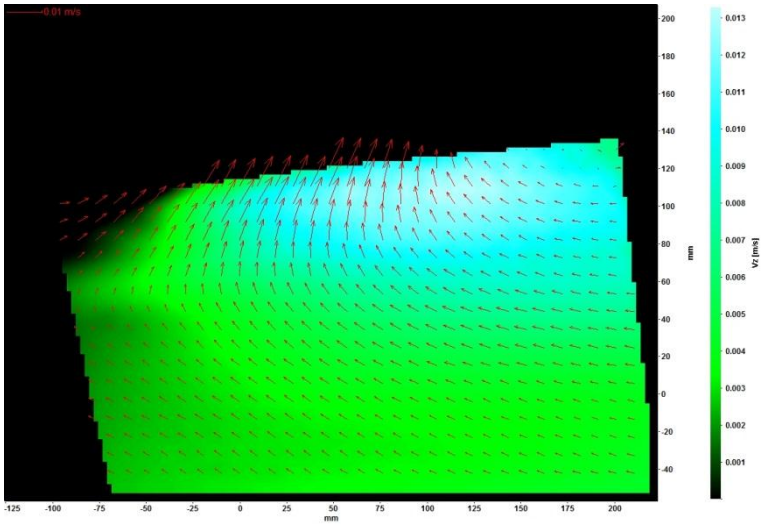

Figure 45. The averaged velocity field of the strong outflow phase

The reference vector value found in the top right corner of the figure 45 is 0.01 m/s. The background color refers respectively to the velocity of the out of plane component. The velocities vary from 0.01 m/s to 0.001 m/s. A larger version of the figure 45 is presented in the appendix I in the figure 2. The averaged velocity field with background image is presented in the figure 46.

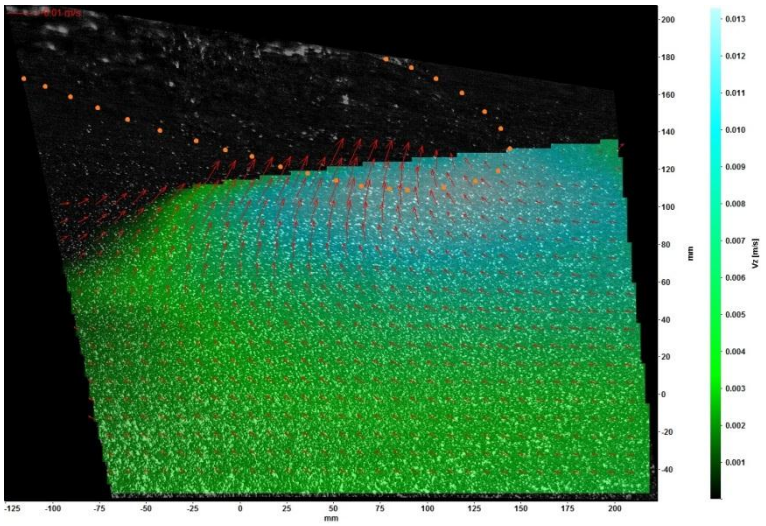

Figure 46. The averaged velocity field of the strong outflow phase with background image

The pipe exit is highlighted with orange dots. Even with missing velocity information due to the geometrical masking it can be said that the inflow is behaving as assumed. The direction of inflow changes from the right side to the left side because of the wall of the blowdown pipe. The time intervals between the same phases were alternating from 0.2 seconds to 1.6 seconds. The maximum length of the stronger inflow phase was 0.8 seconds.

12.3.3 Average vector field of the sideways flow towards the end of the blowdown pipe

The set of 108 velocity field images with indication of sideways flow towards the end of the blowdown pipe (right hand side) was characterized and averaged. The average velocity vector field is presented in the figure 47.

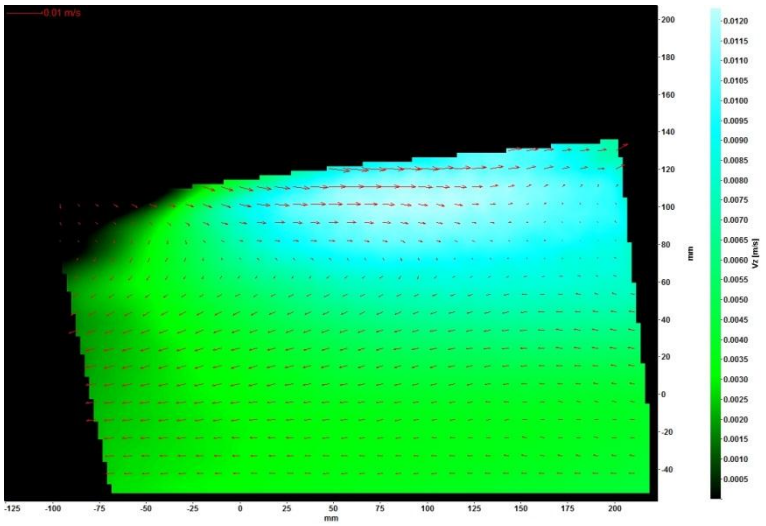

Figure 47. The averaged velocity field of the sideways flow phase

Comparing the velocity field of the sideways flow to previous phases it can be clearly seen that the velocities in the in-plane direction are smaller whereas the out-of-plane velocities are in the same magnitude. The reference vector is in the top left corner of the figure 47. A larger version of the figure 47 is presented in the appendix I in the figure 3. The averaged velocity field with background image is presented in the figure 48.

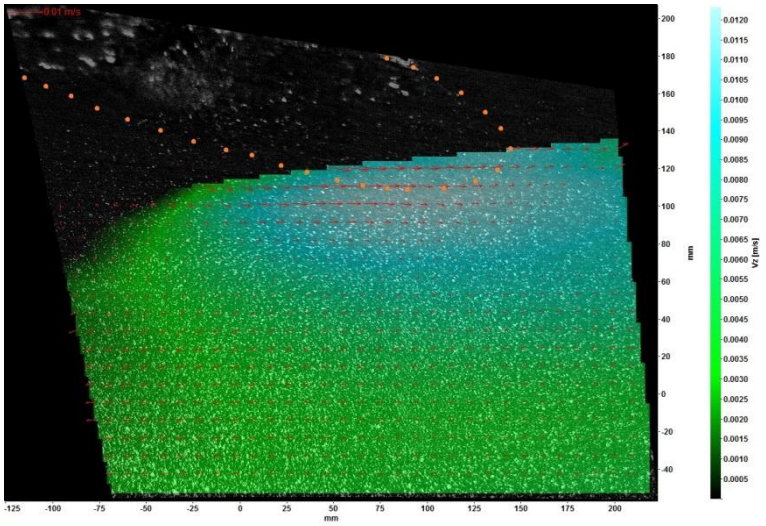

Figure 48. The averaged velocity field of the sideways flow phase with background image

The pipe exit is highlighted with orange dots. It can be assumed that the flow direction turns parallel to the wall of the pipe if the upper regions of the pipe wall would be in the FOV. The time intervals between the same phases were alternating from 0.2 seconds to 4.0 seconds. The maximum length of the sideways flow phase was 1.4 seconds.

12.3.4 Averaged vector field of the vector images indicating swirling underneath the pipe

There were 65 consecutive vector images of the measurement series that had swirls occurring underneath the pipe. The average velocity field of the respective vector images is presented in the figure 49.

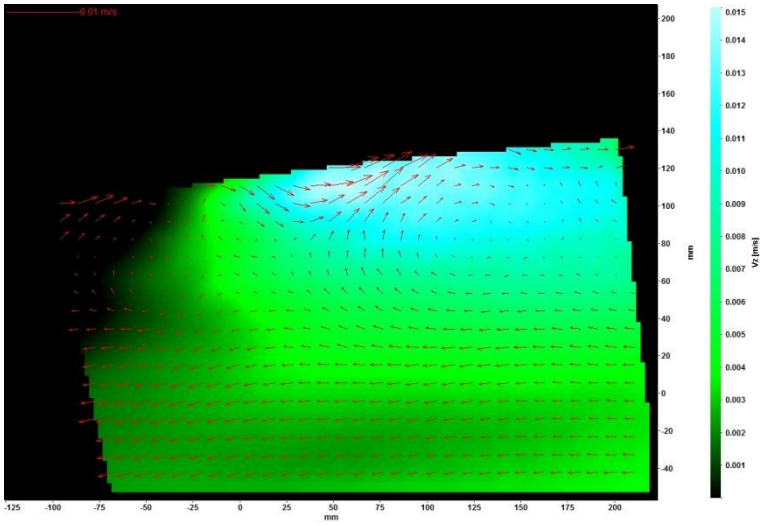

Figure 49. Swirls beneath the exit of the blowdown pipe

There are two distinctive swirls on the left and the right side beneath the exit of the blowdown pipe. The reference vector in the top left corner is relatively larger than in the previous vector field images. The maximum value of the in-plane component is approximately 0.05 m/s and the maximum value of the out-of-plane component is approximately 0.15 m/s. The values of the velocity vectors diminish when approaching the center of the swirls but clear continuous motion can be detected. The swirls appeared for a 13-second period and then vanished. A larger version of the

figure 49 is presented in the appendix I in the figure 4. The averaged velocity vector image with background image and with highlighted outline of the pipe is presented in the figure 50.

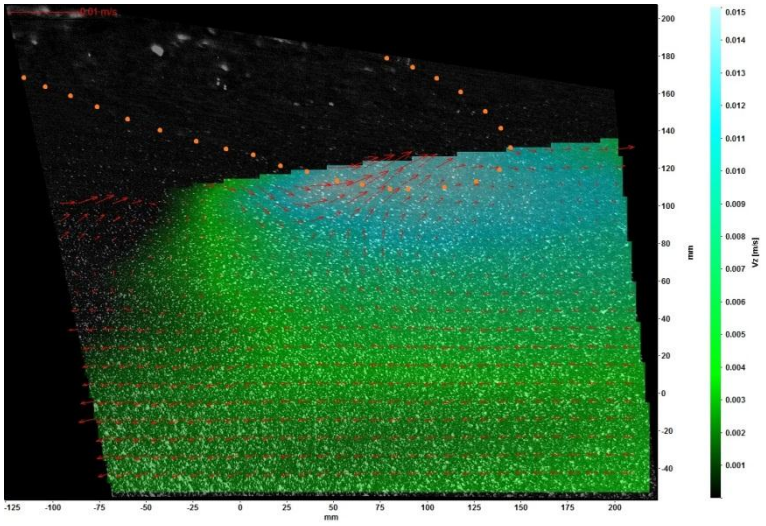

Figure 50. The swirls beneath the pipe with background image

13 CONCLUSIONS

First and the most important conclusion of this thesis is that the acquired PIV system worked like planned and the installation to PPOOLEX was functional. Based on the experience and the results gotten from the preliminary experiments it can be said that PIV is a good addition to the research equipment for Nuclear Safety Research Unit of LUT. PPOOLEX is very challenging environment for PIV but already the preliminary tests showed that good results can be obtained even with existing observation windows. It can also be said that PIV system will be also playing important role in the future studies for Department of Fluid Dynamics. The application might be more suitable for PIV as the flows have constant direction with higher velocities compared with the measurement environment in PPOOLEX.

The biggest restriction for the future studies in PPOOLEX with PIV is the facility itself. The fully free positioning of the PIV system is out of the question because

there are limitations in the amount of observation windows that can be installed into PPOOLEX. In addition there are limitations of positioning observation windows in vertical direction. The horizontal weld of the bottom section of the PPOOLEX is limiting the installing of observation windows higher up from the location where they exist at the moment. Installing new observation windows lower down might not be necessary as there is good view downwards from the blowdown pipe. In future shortening or lengthening of the actual blowdown pipe might come into consideration as it is easier way to change the FOV compared with the installation of new observation windows for cameras. One option to get better free vertical movement of cameras is to make the existing observation windows bigger if it is economically feasible. The observation windows made for lasers are thought to be good enough for the future experiments. The working distance of the laser sheet optics is long enough and there was no problem of illuminating the flow even with lower laser power (around 50% of the maximum pulse energy was used in preliminary testing).

The seeding used in preliminary testing was found out to be suitable for measurements in PPOOLEX. Based on the raw images taken from the experiments seeding density seems to be homogenous. The only problem is that the condensing steam does not contain any tracer particles so the seeding density near the pipe exit will always be lower compared to the parts below the blowdown pipe. This can be substituted possibly by adding more seeding into the pool water before the experiment. The amount of seeding used for preliminary testing was in acceptable level and can be used in the future as the minimum threshold of seeding material. The used seeding material is ideal as its density is close to the water's density and based on the experiments it can be said that seeding follows and reflects well the fluctuations caused by condensation of steam.

When experiments are performed in harsher environment, e.g. the mass flow of the blowdown steam is big enough to cause chugging phenomena in the pipe's exit, the use of laser-induced fluorecense, LIF, should be considered. By using fluorescent dye as a tracer and filters that filter out the wavelength of the laser, the possible

bubbles that reflect the laser light can be filtered out. In principle, only the parts with water containing tracer particles are illuminated in LIF. The practical tests in the future will show if LIF will be feasible for PPOOLEX studies. The biggest problem with LIF could be if the tracer particles are in the boundary layer of the steam bubble thus reflecting light also from the bubbles.

The time delay of the pulses appeared to be suitable when measuring the steam-water interface in the pipe exit. The time delay was set such that a 5-pixel movement of a tracer particle could be detected. The actual frequency of the measurement was 5 Hz and it is close to the maximum frequency that the system is capable of measuring with. Because of the fluctuations caused by condensing of steam did not occur in the regular time interval, it can be said that the phases appear irregularly or the measuring frequency was not high enough to capture all the fluctuations. In the future, the use of external trigger for laser pulses should be investigated. If certain constant pressure changes can be detected, the pulses can be triggered externally resulting in acquiring images of similar flow phases.

The use of PIV can be thought to be very practical. For the most efficient use of the system, experience from different variables and their effect on the results has to be acquired. The general quality of the measurement data will get better as more measurements are done. Already with quite minimal use of the system good results were obtained and it can be said that the quality of the results will get better in the future.

SOURCES

Boaler John. 2011. E-mail discussion.

Hain et al. 2007. Experiments in Fluids Volume. Vol 42, number 3. Springer Berlin/Heidelberg. Journal article.

IEC. 2007. IEC 60285-1, 2nd edition. International Electrochemical Commission. International Standard. 200 pages.

Kasap S. & Capper P. 2006. Handbook of Electronic and Photonic Materials. Springer Science+Business Media Inc. 1406 pages. ISBN 978-0-387-26059-4.

LaVision I. 2007. Flowmaster, Advanced PIV/PTV Systems for Quantitative Flow Field Analysis. Production sheet. 12 pages.

LaVision II. 2008. DaVis, Software for Intelligent imaging. Production sheet. 12 pages.

LaVision III. 2009. Imager Pro X 4M. Production sheet. 1 page.

LaVision IV. 2009. Nd:YAG PIV Laser. Production sheet. 2 pages.

LaVision V. 2011. Light Sheet Optics. Production sheet. 2 pages.

LaVision VI. 2010. Graphic Procession Units. Production sheet. 2 pages.

LaVision VII. 2011. Tender for PIV System to LUT. Tender.

Melling A. 1997. Tracer particles and seeding in particle image velocimetry. Measurement Science and Technology, vol. 8, number 12. IOP Publishing Ltd. Journal article.

Pastila et al. 2009. Ultravioletti- ja lasersäteily. Säteilyturvakeskus. 323 pages. ISBN 978-951-712-502-4.

Laine Jani, Puustinen Markku, Räsänen Antti, Tanskanen Vesa. 2011. PPOOLEX Experiments on Stratification and Mixing in the Wet Well Pool. Lappeenranta University of Technology, Nuclear Safety Research Unit. 25 pages. Research Report.

Raffel M., Willert C.E., Wereley S.T., Kompenhans J. 2007. Particle Image Velocimetry, a Practical Guide. 2nd edition. Springer. 448 pages. ISBN 978-3-540-72307-3.

Turunen-Saaresti Teemu. 2004. Computational And Experimental Analysis of Flow Field In The Diffusers of Centrifugal Compressors. Lappeenrannan teknillinen yliopisto, Digipaino. 95 pages. ISBN 951-764-962-2.

Träger et al. 2007. Springer Handbook of Lasers and Optics. Springer. 1331 pages. ISBN 978-0-387-95579-7.

Westerwheel Jerry. 1993. Digital Particle Image Velocimetry – Theory and Applications Ph.D. Dissertation. Delft University Press, Delft.

Wilson J. & Hawkes J. 1998.Optoelectronics, an introduction. 3rd edition. Prentice Hall. 559 pages. ISBN 0-13-103961-X.

APPENDIX I

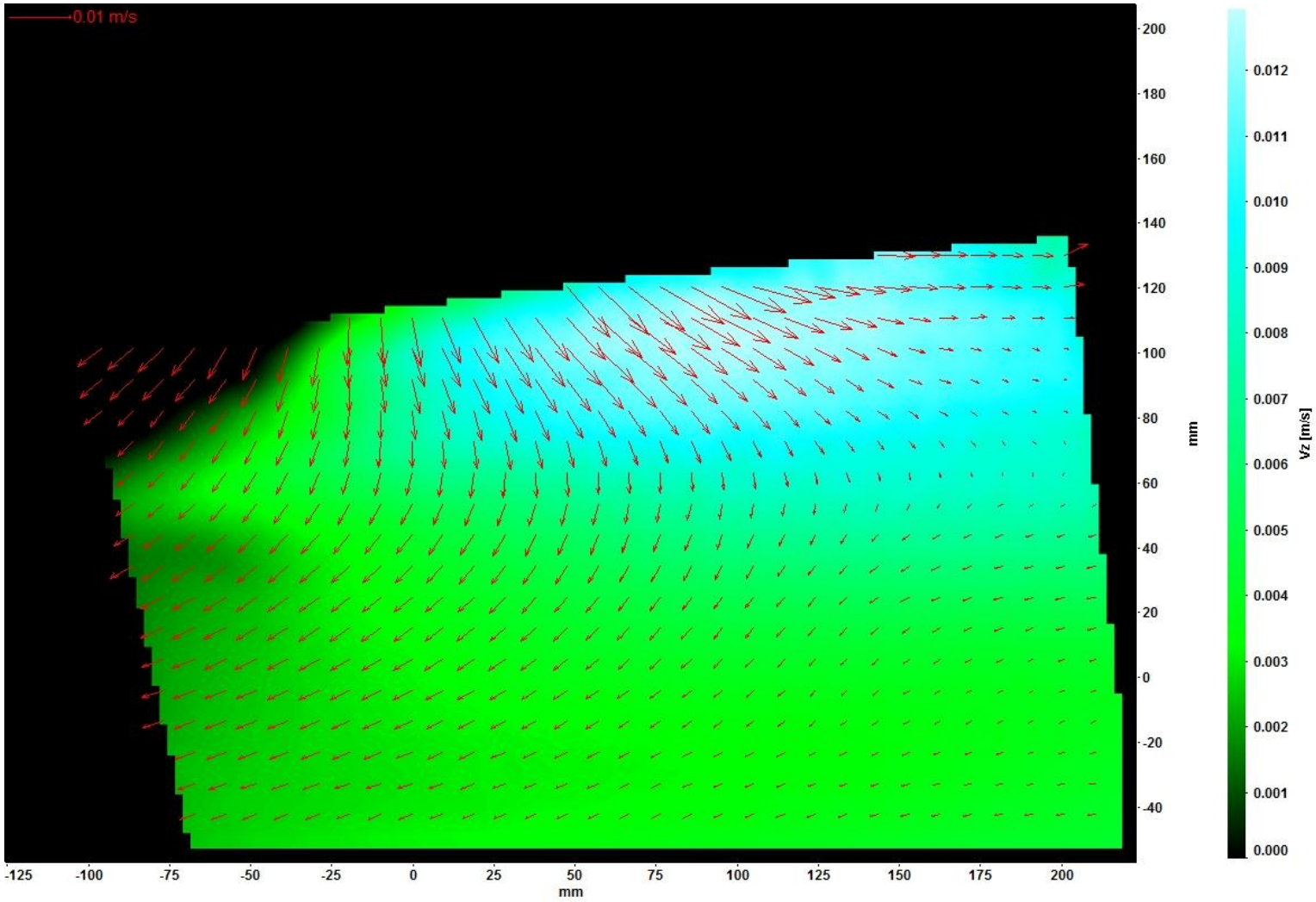

Figure 1. The averaged velocity field of the strong outflow phase

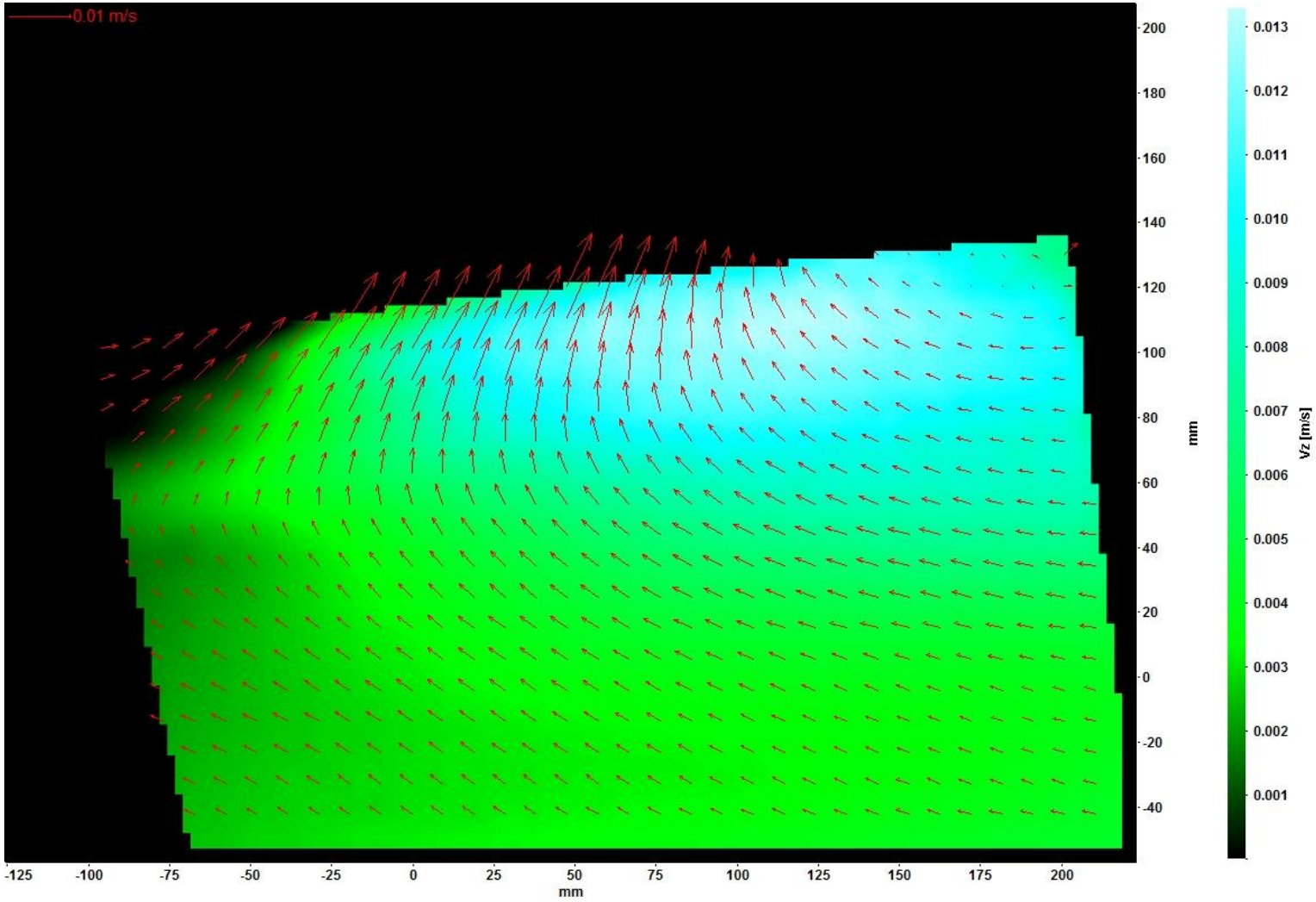

Figure 2. The averaged velocity field of the strong outflow phase

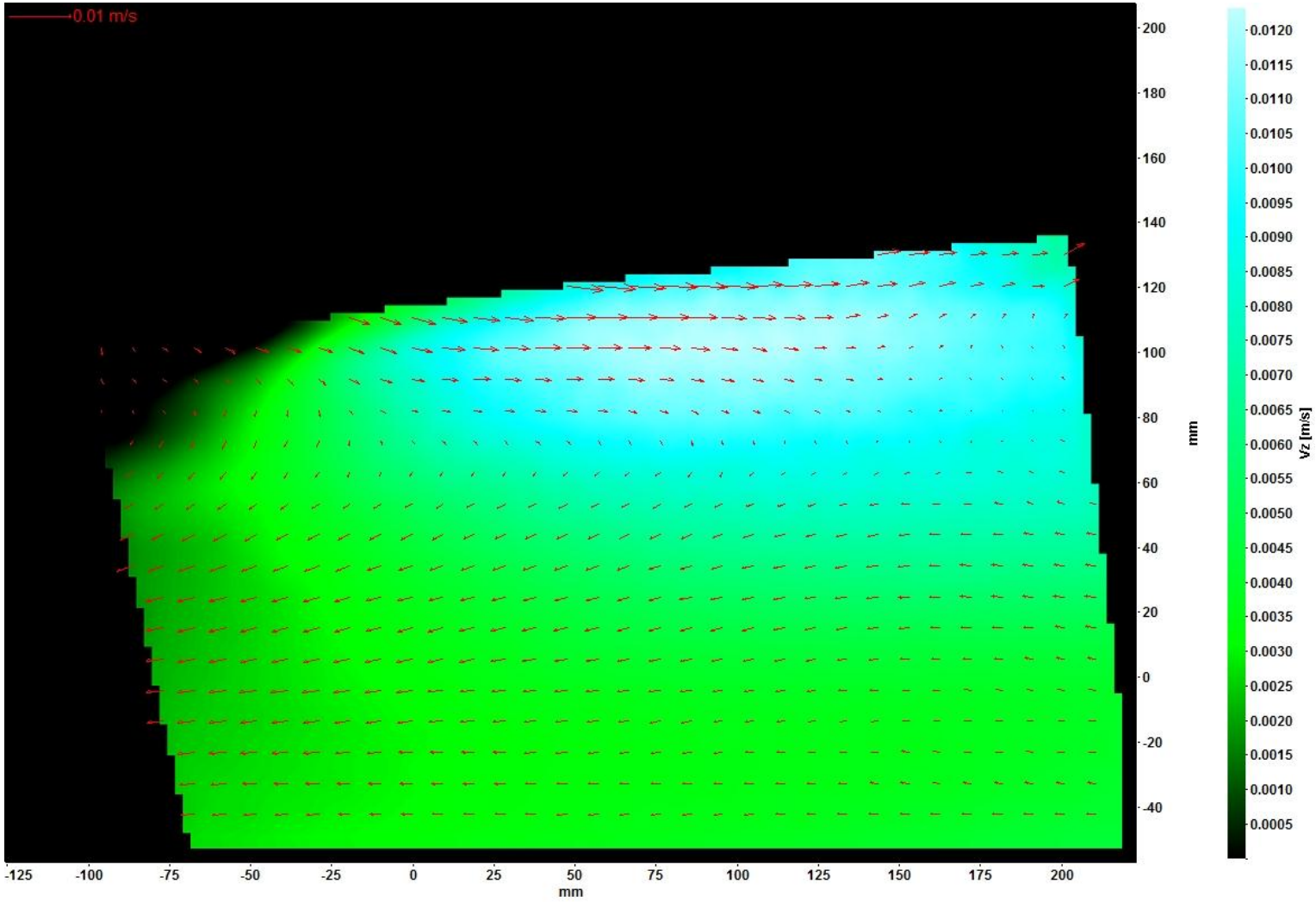

Figure 3. The averaged velocity field of the sideways flow phase

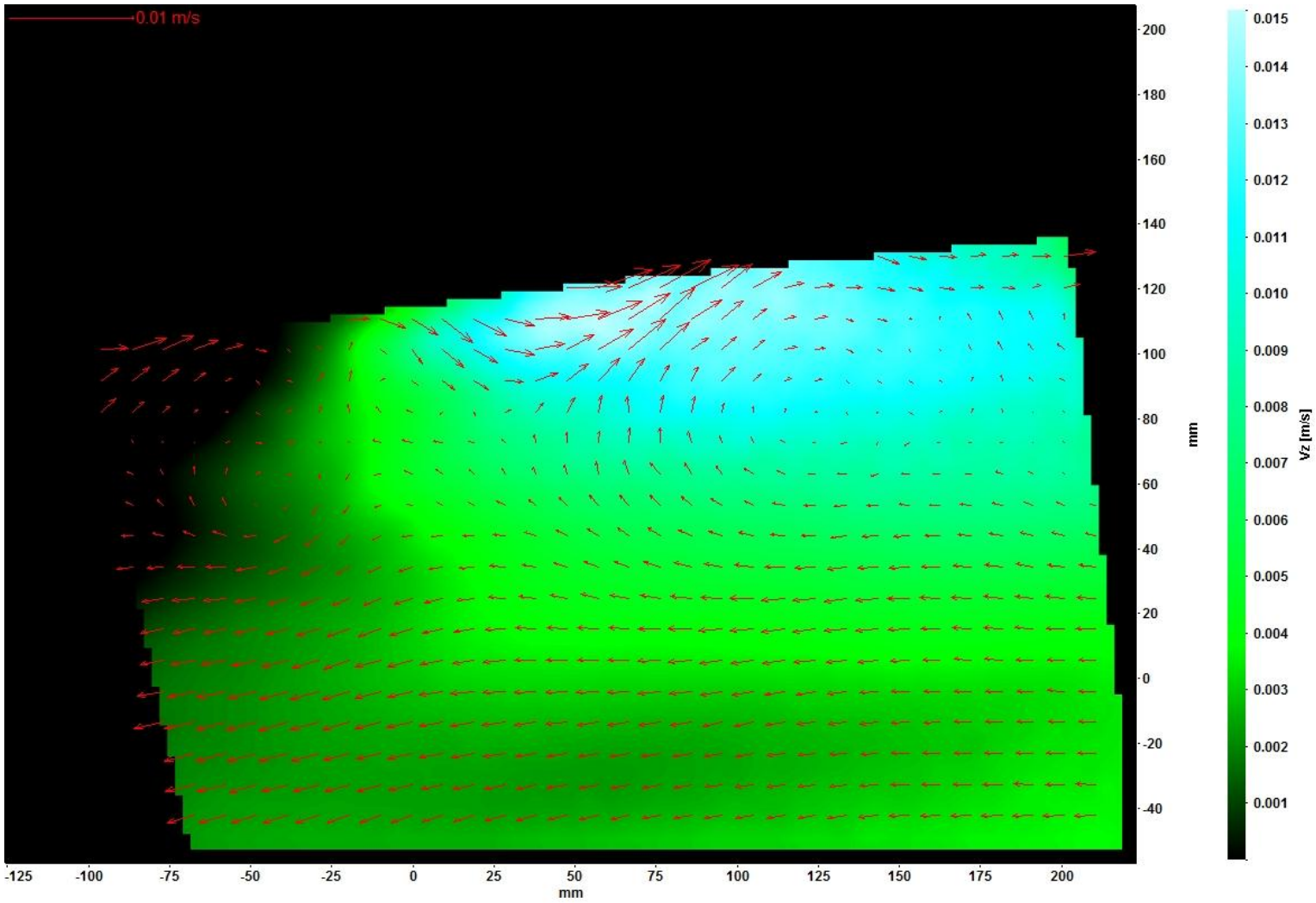

Figure 4. Swirls beneath the exit of the blowdown pipe